Stainless steel wires reinforced ultra-high performance concrete for self-moderating and self-sensing temperature deformations

Stainless steel wires reinforced ultra-high performance concrete for self-moderating and self-sensing temperature deformations

Shuoxuan Ding[1], Sufen Dong[1,*], Ashraf Ashour [2], Xinyue Wang[1], Baoguo Han[1,*]

[1] *School of Infrastructure Engineering, Dalian University of Technology, Dalian 116024, China*
[2] *Faculty of Engineering & Informatics, University of Bradford, Bradford, BD7 1DP, UK*

[*] Corresponding author: dongsufen@dlut.edu.cn, hithanbaoguo@163.com

Abstract

The development of self-moderating and self-sensing concrete composites with high and stable thermal/electrical conductivity is essential to mitigate and monitor the temperature deformation behaviours (TDB) of engineering infrastructures such as highway, bridge pavement, airstrip and ports. Owing to the micron-scale diameter and high aspect ratio, stainless steel wires (SSWs) can establish a comprehensive and extensive thermal/electrical, as well as reinforcing, three-dimensional network within the concrete matrix, even at a low content. This paper thus investigated the TDB self-moderating and self-sensing performances of SSWs enhanced ultra-high performance concrete (UHPC). The main experiments were carried out on SSWs enhanced UHPC slabs, measuring 250 mm×225 mm×16 mm. The volume contents of SSWs studied were 0%, 0.5 vol.%, 1.0 vol.% and 1.5 vol.%. The TDB self-moderating and self-sensing experiments were carried out under different conditions, including indoor and outdoor environments. Such composite showed effective and highly stable capabilities in reducing the temperature difference and diminishing the strain of pavement slabs under different environmental conditions. Compared with the UHPC without SSWs, UHPC with 1.5 vol.% of SSWs can reduce the temperature difference by 7.4 °C (39.4%) when being heated from 21.6 °C to 50 °C, thus, reducing the maximum tensile/compressive strains by 83.1%/82.2%, and the tensile/compressive stresses by 70.8%/82.0%. At a heating rate of 67.1 °C/min, incorporating 1.5 vol.% of SSWs results in significant reductions in both vertical displacement and stress, amounting to 98.6% and 89.6%, respectively. The 1.5 vol.% SSWs reinforced UHPC slab also suppressed 25.0% of temperature difference, 76.6% of strain and 70.7% of stress in scorching outdoor environments. The TDB of SSWs reinforced UHPC can be real-timely reflected by monitoring the quick and small-scale resistance fluctuations, and the fractional changes in resistivity can reach 5.24% with a response time of 0.23 s. The self-moderating and self-sensing performances of such composite remained stable after repeated heating experiments, thus suggesting its potential for promising applications in engineering infrastructures which are susceptible to deformation under high-temperature conditions.

Keywords: Stainless steel wires; Temperature deformation behaviour; Engineering infrastructures; Ultra-high performance concrete; Self-moderating and self-sensing

1. Introduction

The fatigue performance of engineering infrastructures represents a crucial concern, with deformations resulting from temperature differences potentially contributing up to 22% of the cumulative fatigue damage index of pavement slabs over 35 years of use [1]. Moreover, temperature-induced deformation can lead to misalignment among pavement slabs, internal cracking of engineering infrastructures, and even sidewall collapse during underground constructions [2-4], thus inducing serious safety accidents. Under these circumstances, timely implementation of self-moderating and self-sensing mechanisms to monitor temperature deformation behaviour (TDB) is an essential task for engineering infrastructure maintenance [5-8]. However, the timely detection of such deformations poses a considerable challenge when relying on conventional methods [9,10]. Furthermore, employing high-precision equipment for detection not only incurs significant expenses but also contributes significantly to carbon dioxide emissions [11]. Self-moderating materials represent a category of functional materials capable of autonomously adjusting their working performance, such as their own temperature and humidity to suit the environment and adapt their shape to the outer space. Such moderating materials overcome the shortcoming of conventional methods that need to be updated multiple times throughout the whole life cycle of engineering infrastructures.

On one hand, there are fairly few experimental research studies focused on mitigating the TDB of concrete infrastructures. Liao et al. [12] used lightweight sand as a carrier for phase-change materials (PCM) to optimise the thermal curling of concrete slabs, as the incorporation of PCM can bring a latent heat of fusion of approximately 21 J/g. However, conventional PCM showed much lower thermal conductivity than concrete materials, causing a lag in temperature transfer at the bottom of concrete slabs. This lag can lead to substantial temperature variations between the two surfaces of engineering infrastructure slabs, thus aggravating the TDB [13]. Besides, the density of engineering infrastructures might be reduced due to the lower density of the porous/polymeric carrier and PCM compared to common aggregates, consequently contributing to reduced strength of engineering infrastructures. In another study, Belshe et al. [14] employed an asphalt rubber material to construct a 19-mm friction course on the engineering infrastructures, aiming to lessen the temperature difference between the top and bottom of the slab by 1–3 °C. Such open-graded friction course utilisation can improve the aeration effect as traffic travels through, thus accelerating the heat transfer between the pavement slabs and the surrounding air. However, the reducing effect on temperature difference was not significant enough and the mitigation of curling stress was also less pronounced. Moreover, since the friction course was formed from an asphalt rubber material, it exhibited greater susceptibility to deformation than concrete engineering infrastructures, potentially leading to unexpected damage [15,16].

On the other hand, the available methods for sensing the TDB of engineering infrastructures are also limited and costly. Zhu et al. [17] introduced a self-developed temperature stress testing system for determining the TDB of mass concrete, but the equipment size was too large for practical and widespread applications. Azenha et al. [18] used plastic and metal vibrating wire strain gages to monitor the temperature and strain of early-aged concrete, concluding that plastic vibrating wire strain gages with low stiffness were more suitable to measure the TDB. However, the plastic strain gages exhibited higher thermal sensitivity in the pre-solidarization period, leading to measured total strains that were higher than the actual values. Liao et al. [19] embedded fibre-optic sensors within concrete engineering infrastructures to measure temperature and strain, and also employed optical fibre inclinometer as tilt angle sensors. While the fibre optic sensors displayed efficient and accurate measurement results, with ample data types, the associated expenses were quite considerable and the construction process was complicated.

Thus far, no research has simultaneously addressed the TDB mitigation and monitoring of engineering infrastructures, let alone the TDB self-moderating and self-sensing of the engineering infrastructures [20]. Characterized by outstanding strength, superb toughness and super-high durability, ultra-high performance concrete (UHPC) is popularly employed in engineering constructions, especially in engineering infrastructures. Meanwhile, the excellent crack resistance and high durability of UPHC contribute to a longer service life of engineering infrastructures. Notably, the elimination of coarse aggregate when producing UHPC prevents the disconnection of thermal and electrical conduction paths caused by large-sized coarse aggregate. Therefore, the speed of heat transfer inside UHPC engineering infrastructures is much faster than that of ordinary concrete pavement. Together with the superb compactness and extremely low porosity, engineering infrastructures made of UHPC can maintain steady thermal and electrical conductivity over an extended service life [21].

The commonly employed functional fillers for achieving self-moderating and self-sensing UHPC are generally divided into 2 types [22]: powdered (e.g., steel powder [23,24], carbon black [25,26], graphite powder [27,28], graphene [29,30], nickel powder [31,32], carbon nanotubes [33,34]) and fibrous (e.g. carbon fibre [35,36], steel fibre [37,38]). However, the highly compact internal microstructure of UHPC poses challenges to the effectiveness of powdered functional fillers as they are tiny in size and easily coated by hydration products, preventing them from forming a connected thermal conductive network at low concentrations [39-41]. Conversely, high concentrations of powdery functional fillers lead to poor dispersion and increased agglomeration, thereby reducing the strength of UHPC [42]. On the other hand, the commonly used fibrous functional fillers mentioned above have also shortcomings. Steel fibres, with large diameters and high density, fail to satisfy the percolation threshold at a low content [38,43]. Nevertheless, higher contents of steel fibres have adverse effects on the fluidity of the mixture and introduce pores or other defects into the UHPC matrix. Furthermore, steel fibres are prone to rusting, undermining long-term stability. The interface of carbon-based fibres and the UHPC matrix is fragile, potentially weakening the strength of the developed composite. Moreover, carbon fibres exhibit poor thermal and electrical conductivity, often requiring a fairly high content to achieve desirable working efficiency. Stainless steel wires (SSWs) offer an alternative solution to enhance the thermal and electrical conductivity of the UHPC matrix. The micron-scale diameter and high aspect ratio of SSWs enable it to constitute a comprehensive and extensive thermally and electrically as well as reinforcing three-dimensional network within the UHPC matrix at a fairly low dosage, thereby empowering the UHPC structure with outstanding mechanical, thermal and electrical properties [8,44]. Existed studies [11,45] have shown that SSWs can effectively improve the electro-thermal properties, wear resistance, and dynamic/static impact resistance of the UHPC structures, thereby demonstrating promising potential for long-term stable service under high-load traffic intensity (including heavy aircraft and special vehicles etc.). Furthermore, compared with carbon fibres and steel fibres, SSWs can ensure excellent self-moderating and self-sensing performances at greatly reduced contents, from tens of percent down to 1.5 vol.% [46]. In addition, its stainless property and ultra-high durability enable it to sharply decline the cost during the whole life cycle.

Therefore, this paper focuses on verifying the feasibility of incorporating SSWs to enhance UHPCs for fabricating TDB self-moderating and self-sensing composites. The self-moderating and self-sensing capacity as well as the stability of SSWs enhanced UHPC slabs (measuring 250 mm×225 mm×16 mm) were evaluated.

2. Theoretical analysis and testing method

2.1 Theoretical solution of temperature deformation behaviour

According to the Westergaard temperature deformation method [47], the temperature is nonlinearly distributed in the plane of the pavement slab and through its thickness. Additionally, in compliance with the Specifications for Design of Highway Cement Concrete Pavement [48], the strains at any surface point of the slab can be calculated through Eq. (1):

$$\begin{cases} \varepsilon_x = \dfrac{1}{E_c}(\sigma_x - \mu\sigma_y) + \alpha\Delta t \\ \varepsilon_y = \dfrac{1}{E_c}(\sigma_y - \mu\sigma_x) + \alpha\Delta t \end{cases} \tag{1}$$

where ε_x and ε_y are strains along the transversal and longitudinal directions of the point, E_c is the elastic modulus of the pavement slab (MPa), σ_x and σ_y are stresses along the transversal and longitudinal directions of the point (MPa), and μ is the Poisson's ratio of the slab. The parameter α represents the coefficient of linear thermal expansion (°C^{-1}), and Δt is the temperature difference between two surfaces of the pavement slab (°C).

For temperature stress, it can be calculated by Eq. (2):

$$\begin{cases} \sigma_x = \dfrac{E_c \alpha \Delta t}{2(1-\mu^2)} \cdot (C_x + \mu C_y) \cdot D_x \\ \sigma_y = \dfrac{E_c \alpha \Delta t}{2(1-\mu^2)} \cdot (C_y + \mu C_x) \cdot D_y \end{cases} \tag{2}$$

where C_x and C_y are warping stress coefficients of transversal and longitudinal directions, D_x and D_y are intra-temperature stress coefficients considering the nonlinear distribution of temperature gradient. Complementary, $C_{x,y}$ and $D_{x,y}$ (i.e., C_x, C_y, D_x and D_y, respectively) are referred to the following Eqs. (3) to (6):

$$C_{x,y} = 1 - \frac{\sin h\beta \cos\beta + \cos h\beta \sin\beta}{\cos\beta \sin\beta + \sin\beta \cos h\beta} \tag{3}$$

$$\beta_{x,y} = \frac{\sqrt{2} L_{x,y}}{4 l_0} \tag{4}$$

$$D_{x,y} = 1.77 e^{-4.48h} C_{x,y} - 0.131\left(1 - C_{x,y}\right) \tag{5}$$

$$l_0 = \sqrt[4]{\frac{E_c h^3}{12(1-\mu^2)k}} \tag{6}$$

where h is the thickness of the pavement slab (cm), $L_{x,y}$ is the size parameter of the pavement slab, $\beta_{x,y}$ reflects the relationship between h and l_0, and l_0 is the radius of the relative stiffness of the Winkler subgrade model (cm), and k is the subgrade reaction modulus (MPa).

2.2 Raw materials and mix proportion

The raw materials used in this investigation were Portland cement (PC), silica fume (SF), fly ash (FA), quartz sand (QS), water, water reducer and SSWs. The content of each raw material and the strength [44] of the fabricated UHPC are displayed in Table 1. The type of PC used for preparing the testing slabs was P·O 42.5R. The type of SSWs was 316L, having a length of 10 mm, a diameter of 20 μm, and the tensile strength and thermal conductivity were 780 MPa and 16.2 W/(m·K) respectively. The QS had a particle size ranging from 0.12 to 0.83 mm. The SF with an average diameter of 150 nm contained 94.2% SiO_2, and the FA (class F) had a specific surface area of 0.08-1.95 m^2/kg. The water reducer applied in this study was a polycarboxylate superplasticizer (provided by Sika Co. Ltd.), which can endow the fresh mixture with splendid workability. The volume contents of SSWs used in this study were 0%, 0.5 vol.%, 1.0 vol.% and 1.5 vol.%, corresponding to slabs labelled as W0, W0.5, W1.0 and W1.5 respectively.

Table 1 Content of each raw material and the strength of fabricated UHPC.

Specimen	Content of each raw material/(kg/m^3)							Strength/MPa
	PC	FA	SF	QS	Water	Water reducer	SSWs	
W0	783.3	195.9	245.0	1076.7	293.9	11.8	0	~102.5
W0.5							46.9	~121.4
W1.0							93.9	~154.9
W1.5							140.7	~174.6

2.3 Preparation process

The preparation process in this study followed the guidelines provided in reference [49]. A mixer with 2 stirring speeds was used to prepare the fresh mixture. The higher speed was up to 285 ± 10 $r \cdot min^{-1}$ and the lower speed was 140 ± 5 $r \cdot min^{-1}$. The preparation method was consistent with Fig.1.

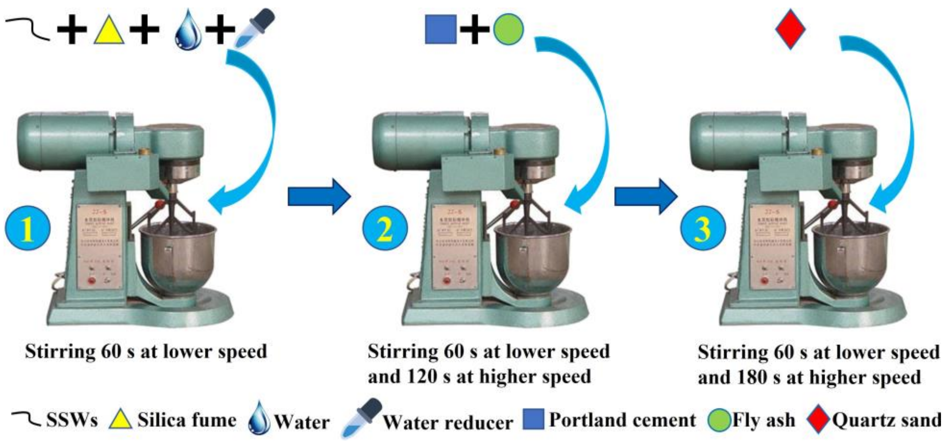

Fig. 1. Preparing process of testing slabs.

The test specimen mould, with a size of 250 mm × 225 mm × 16 mm was lightly coated with oiled, and a fresh mixture of UHPC was poured into the mould. The concrete vibrating table was used to discharge air within the mixture, vibrating 2860 times per 1 minute with an amplitude ranging from 0.3 mm to 0.6 mm. The mould with the mixture was positioned on the vibrating bench for 2 min until the surface of the slab was smooth. Subsequently, all testing slabs were placed in a standard curing room for 24 hours, and, then, they were demoulded and cured until being tested.

2.4 Experimental procedures

The bridging effect of SSWs and their uniform dispersion within the UHPC matrix was observed by using scanning electron microscopy (SEM). The strain data were collected by a distributed stress-strain testing and analysis system (Model DH3820) with strain gauges (wire grid sized 20 mm × 3 mm). During strain data collection, a sampling frequency of 5 Hz was employed, and temperature compensation strain gauges were used for self-compensation at every measuring point. Temperature measurements were conducted by thermocouples and thermometers (Model K). Electrical resistance data were gathered by adopting the two-electrode-DC method, with a Keithley 2100 Digital Multi-function Meter. Besides, the 287-L20 model thermal imager was employed to take thermograms. The heat resources applied in this study were digital heating stages and infrared heating lamps. The digital heating stage, model BY3030, featured a working surface of 300 mm × 300 mm, is capable of being heated to a target temperature at constant power and then maintaining that temperature. The infrared heating lamp was utilized to simulate the sunlight exposure. The input power was 500 W per lamp-tube (quartz walled, with a length of 350 mm), and each infrared heating lamp contained 2 lamp tubes.

The TDB self-moderating and self-sensing experiments were carried out under different conditions, as detailed in Table 2. In all experiments, only one surface of the slab received heat energy from the heat sources. Thus, the heated surface was labelled as HS, while the unheated surface was denoted as UnHS.

Table 2 Experimental conditions and code names

Types of experiments	Experimental sites	Heating resources	Code names
TDB moderating	Indoors	Digital heating stage	M1
		Infrared heating lamp	M2
	Outdoors	Solar energy	M3
TDB sensing	Indoors	Infrared heating lamp	S

Figure 2 illustrates the configuration of SSWs and arrangement of measuring points. In Fig. 2(a), the length and diameter of discrete SSWs are clearly displayed. Fig. 2(b) indicates that the longitudinal and transversal dimensions of the slab were 225 mm and 250 mm, respectively. The temperature and strain were measured by using thermocouples and strain gauges, respectively. Thermocouples placed at the centre point, the quatre corner and the corner of HS were denoted as X1, X2 and X3, while those arranged at the same positions of UnHS were labelled as X4, X5 and X6. Strains are measured using the half-bridge method to eliminate errors, which are induced by the deformation of strain gauges under sharp temperature changes. Two strain gauges are arranged at each measuring point, namely the working gauge and the compensation gauge. The strain gauges were positioned at the quatre corner, the centre point, the midpoint of the transversal side and the midpoint of the longitudinal side of the slab, denoted as Y1, Y2, Y3 and Y4 respectively. For strain measuring points with two mutually perpendicular strain gauges (Y2, Y3 and Y4), the gauges were distinguished by being labelled as transversal or longitudinal. The vertical displacement of the slab corner was monitored only in the M2 series of experiments by using a linear variable displacement transducer (LVDT), marked as L, as shown in Fig. 2(c). Since each slab can be divided into four symmetrical rectangles, and the temperature-induced deformation trends of these four rectangles are basically the same, vertical displacement only needs to be measured by using LVDT at just one corner of the slab. In order to avoid the error induced by a single measurement, the value of vertical displacement is averaged from three cyclic experimental results.

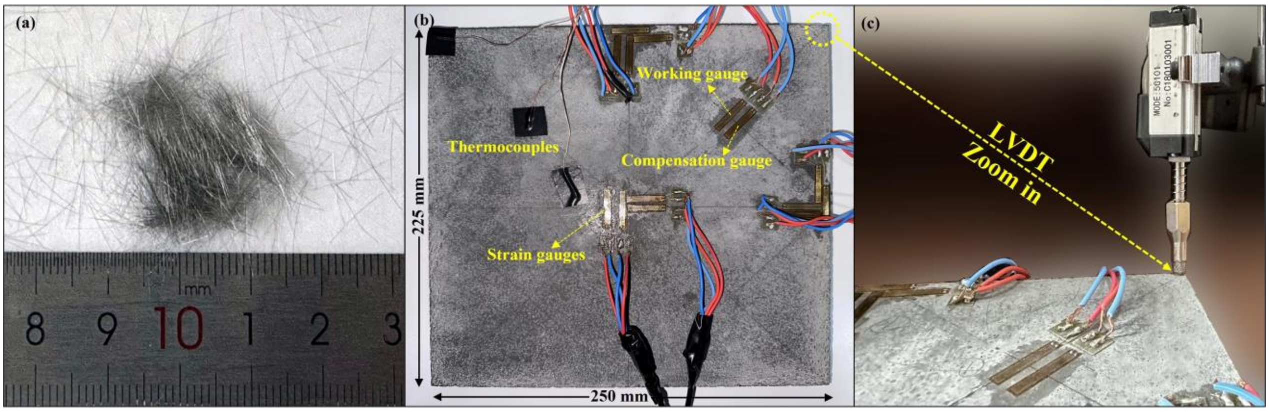

Fig. 2. Configurations of SSWs and arrangement of measuring points: (a) Configuration of SSWs; (b) Arrangement of strain gauges and thermocouples; (c) Zoomed-in figure of LVDT.

As displayed in Fig. 3(a)-Fig. 3(c), the slabs were encased in a layer of expanded polyethene (EPE) foam during experimental processes. In this configuration, only one surface of the slab can receive heat energy from heat sources, thus ensuring that the heat energy is transferred along the thickness of the slab. When conducting the M1 series of experiments, the target temperatures of the digital heat stage were set at 50 °C, 65 °C and 80 °C, respectively, marked as T1, T2 and T3. To control different heating rates during the M2 and S series of experiments, the distances between the infrared heating lamp and HS were determined as 100 mm, 150 mm and 200 mm, which were, respectively, marked as D1, D2 and D3. The average heating rates of D1, D2 and D3 were 67.1 °C/min, 20.1°C/min and 11.0 °C/min, respectively. When conducting the S series of experiments, a 10 mm-wide copper foil tape was affixed along the transversal side of the slab, and two transversal side surfaces were covered with the tape to precisely measure the electrical resistance of the slab, as shown in Fig. 3(d). The number of cyclic experiments was marked out by using the letter K. Hence, according to the nomenclature mentioned above, M1-W1.5T2K2 indicated the second cyclic M1 experiment conducted on the W1.5 slab with the target temperature of 65 °C, M2-W0.5D3K1 represented the first cyclic M2 experiment carried on the W0.5 slab with the distance between infrared heating lamp and HS of 200 mm, and S-W1.0D1K3 denoted the third S series of experiment conducted on the W1.0 slab with the distance between infrared heating lamp and HS of 100 mm. Before each experiment, the heating resources were preheated for 5 min to ensure that the heat release was stable and uniform during the experimental process, and the data of temperature, strain, vertical displacement and electrical resistance were collected synchronously in the corresponding experiments.

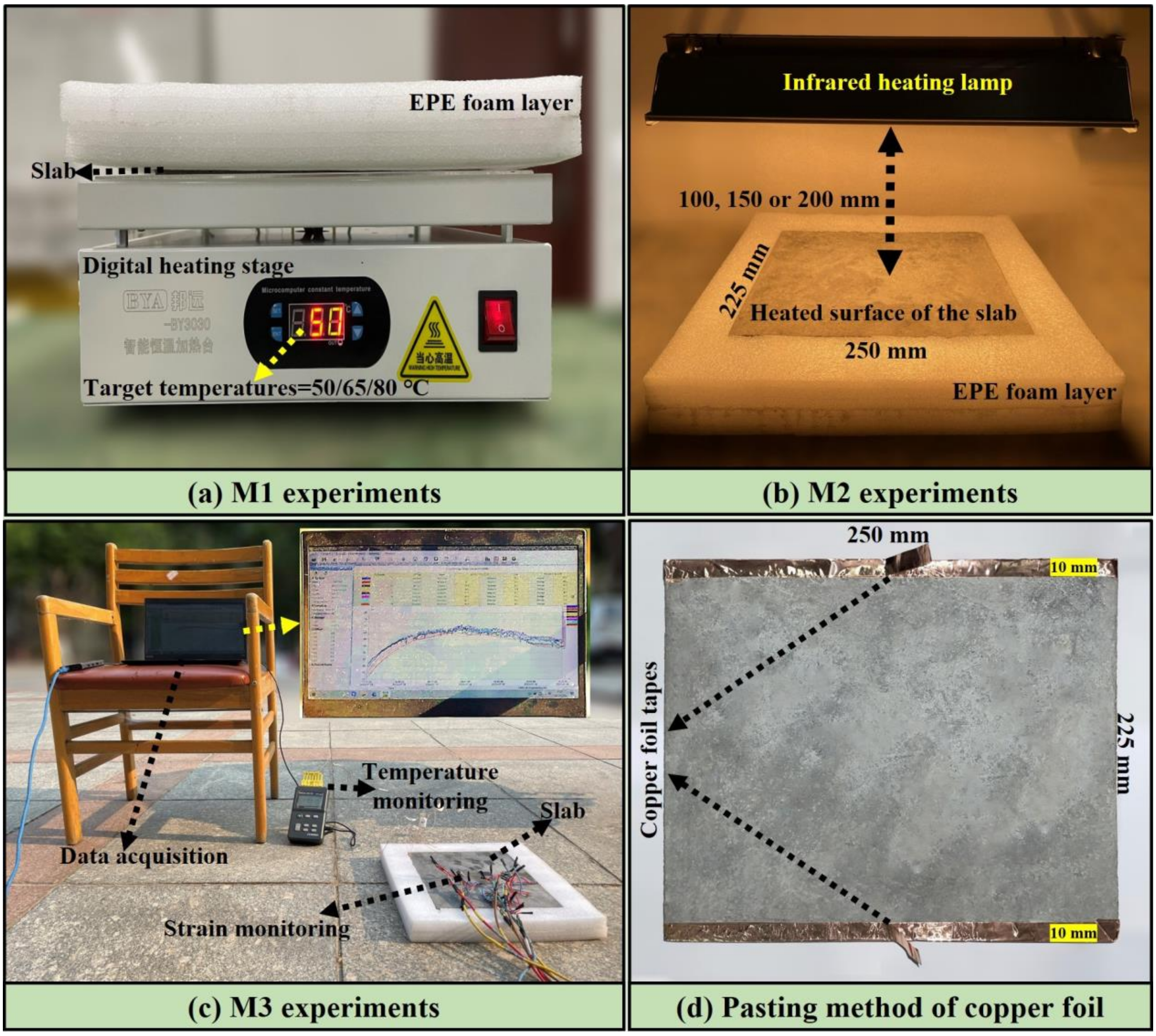

Fig. 3. Schematic diagram of experimental setups.

3. Results and analysis

3.1 TDB self-moderating performance

3.1.1 Self-moderating performance under different target temperatures

Fig. 4 exhibits the thermography of the slab in M1 experiments. It is quite evident that the temperature of the slab gradually decreases from the centre to the corners, consistent with the findings in the references [12,19]. As the heat exchange with the surrounding air in the corner areas of the slab is much more frequent than in the centre of the slab, the surface temperature distribution of a pavement slab is not entirely uniform under actual conditions, especially at the bottom of the slab. In addition, with the development of target temperature, this phenomenon becomes more pronounced.

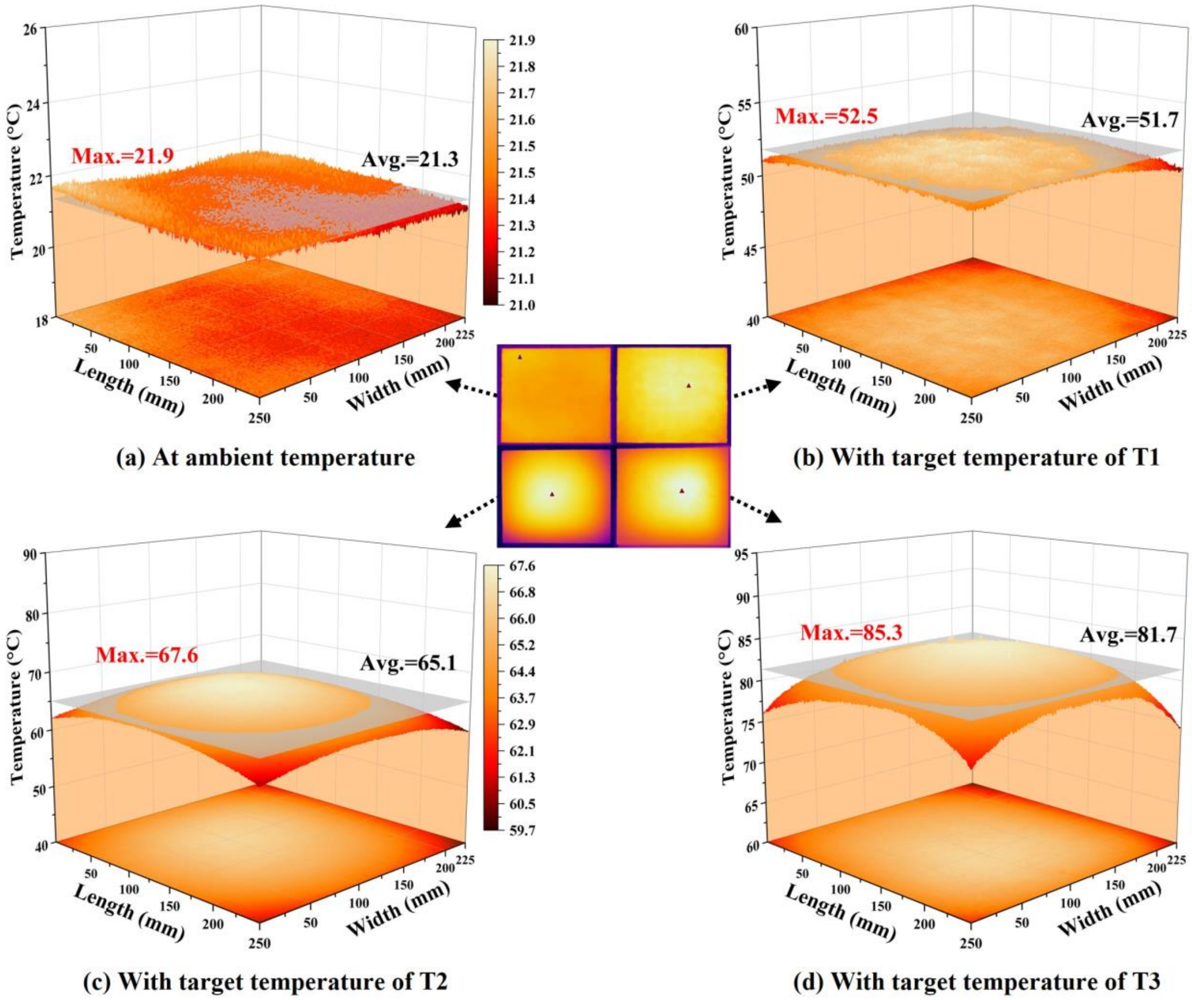

Fig. 4. Thermography of the slab in M1 experiments.

Figs. 5, 6 and 7 illustrate the temperature-time histories of 3 target temperatures in M1 experiments. These figures clearly demonstrate that the trends of curves are highly consistent across different target temperatures and different slabs. The temperature of X3 is lower than that of X1 and X2 during the heating process. The heating processes of the slabs are divided into 2 nonlinear phases, and the heating rates change from high to low. This is because, with the increase in surface temperature, the heat liberation rate of the slab is greater than its absorption rate. In addition, the maximum temperature difference appears at the time point where the heating rate changes. Besides, the heating rate of UnHS develops with the increase of SSWs contents, indicating that the addition of SSWs can effectively improve the thermal conductivity of the slabs.

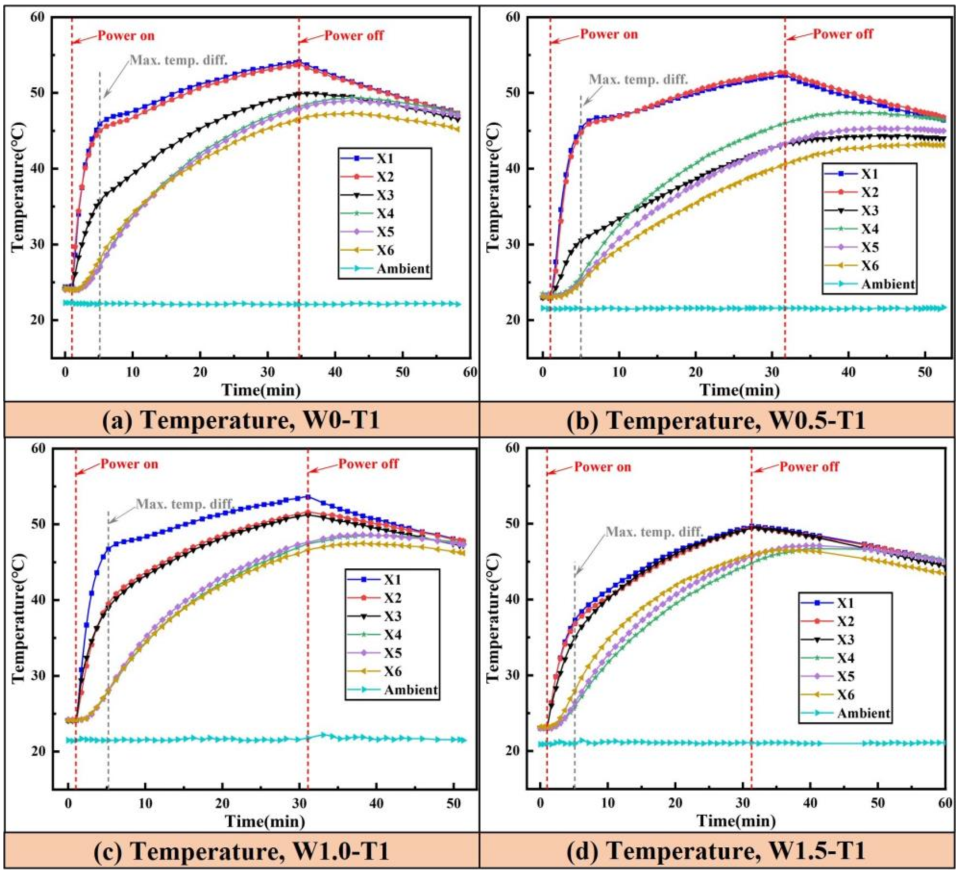

Fig. 5. Temperature time histories of M1-T1.

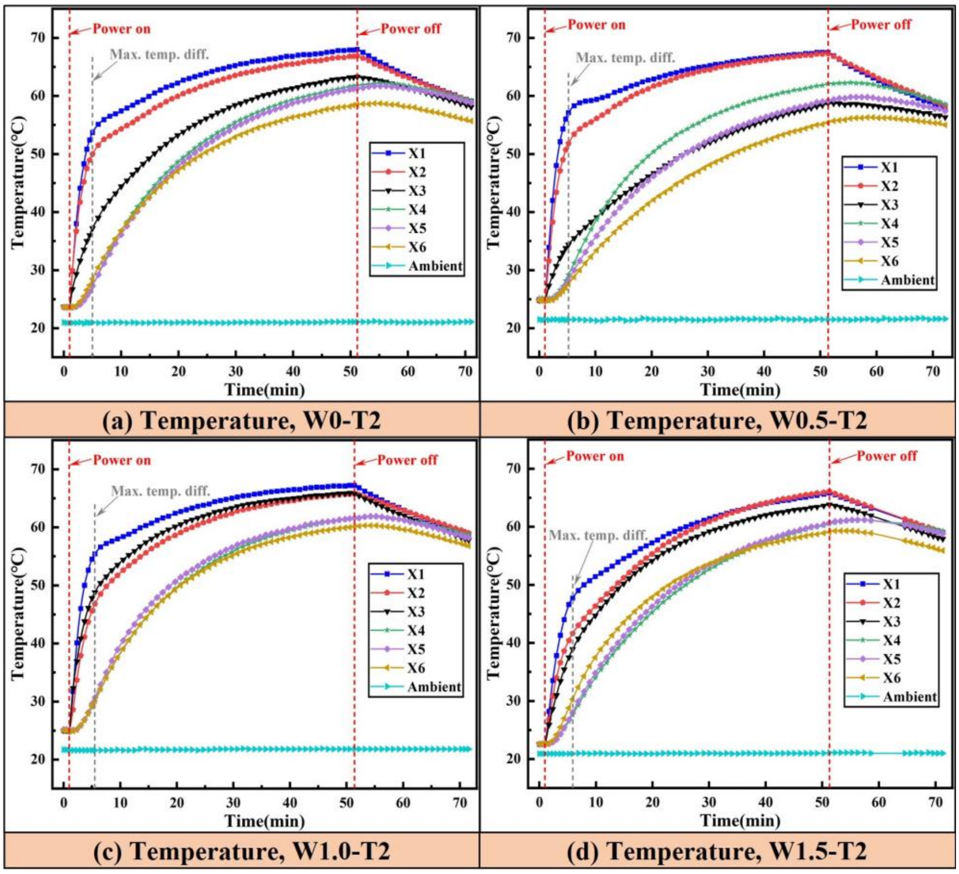

Fig. 6. Temperature time histories of M1-T2.

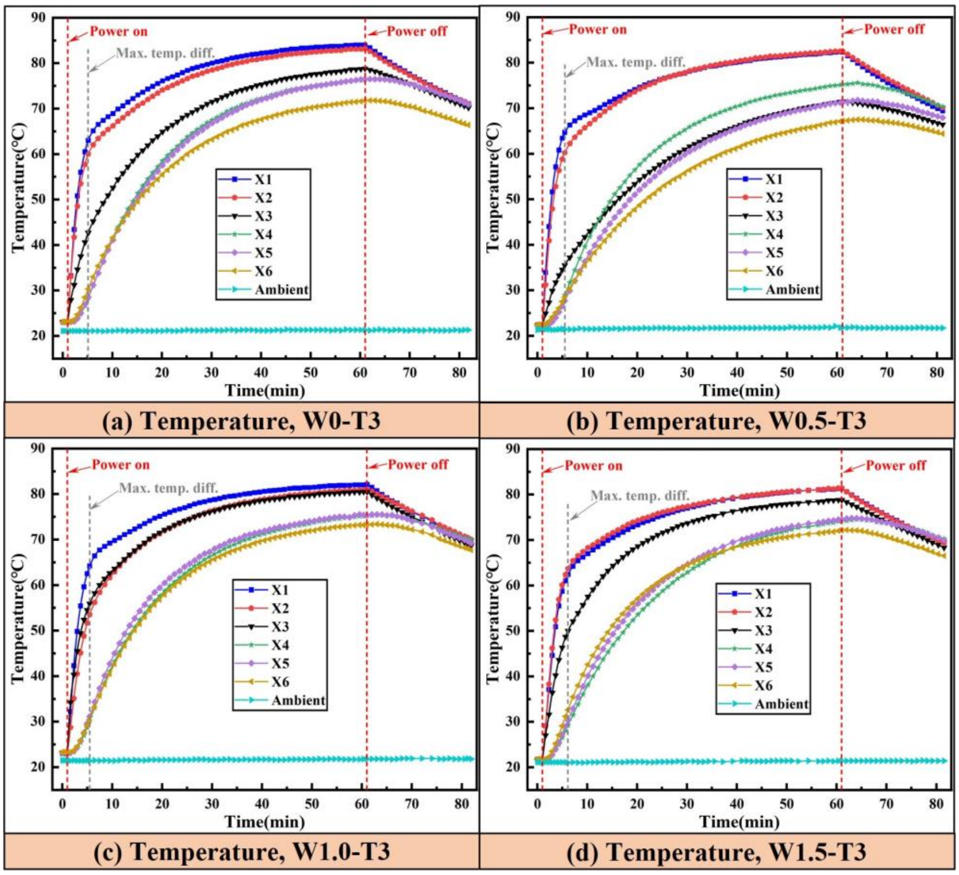

Fig. 7. Temperature time histories of M1-T3.

Figs. 8 to 10 reflect the temperature differences of three target temperatures in M1 experiments. The three figures reveal that the temperature difference of X3-X6 is much lower than that of X1-X4 and X2-X5, this phenomenon also stems from the low temperature of X3 shown in Figs. 5 to 7. Incorporating 0.5 vol.% of SSWs cannot show a significant impact on reducing the temperature differences. This low impact may be attributed to the insufficient quantity of SSWs, which are not able to form a comprehensive thermally conductive network within the UHPC matrix. Additionally, the addition of 1.5 vol.% of SSWs into the UHPC matrix results in a sharp decrease in the temperature differences: dropping by 39.4% (7.4 °C), 23.9% (6.3 °C) and 4.3% (1.5 °C) under the target temperature of T1, T2 and T3, respectively. This phenomenon is oriented from the bridging effect of SSWs (shown in Fig. 11), where the high content of SSWs can overlap and bridge each other, forming an extensive three-dimensional thermal and electrical network. This greatly improves the thermal and electrical conductivity of the UHPC, thereby accelerating the heat transfer along the thickness direction of the slab.

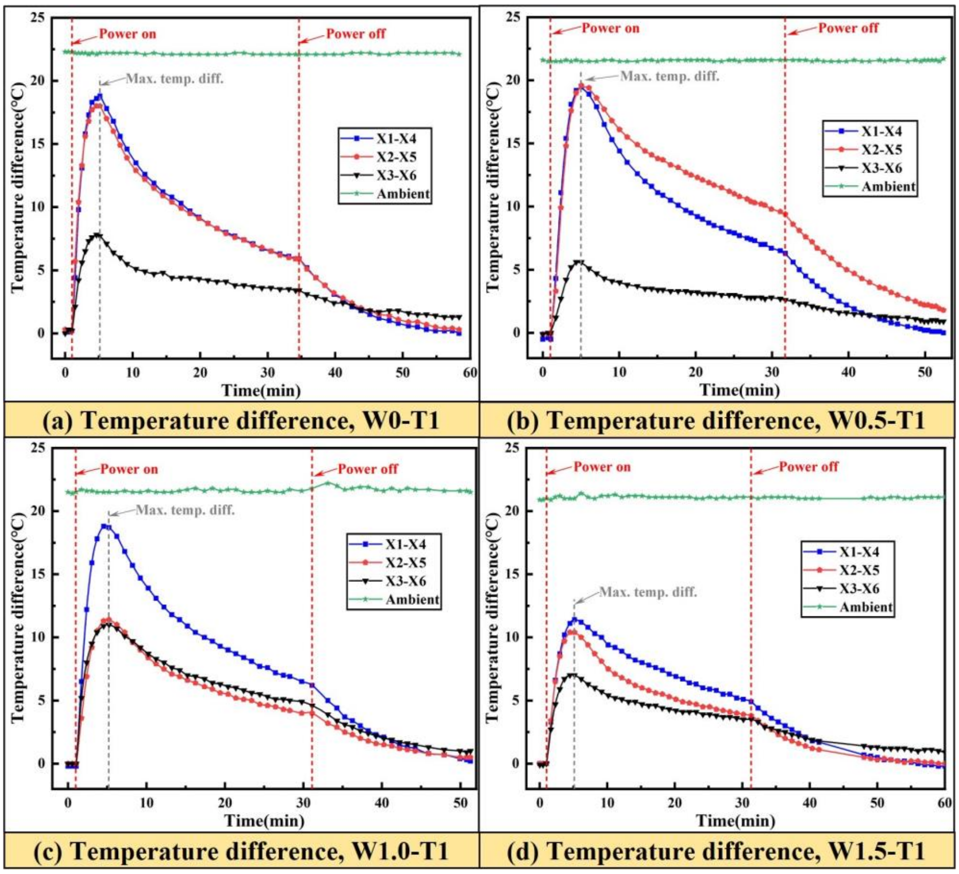

Fig. 8. Temperature differences of M1-T1.

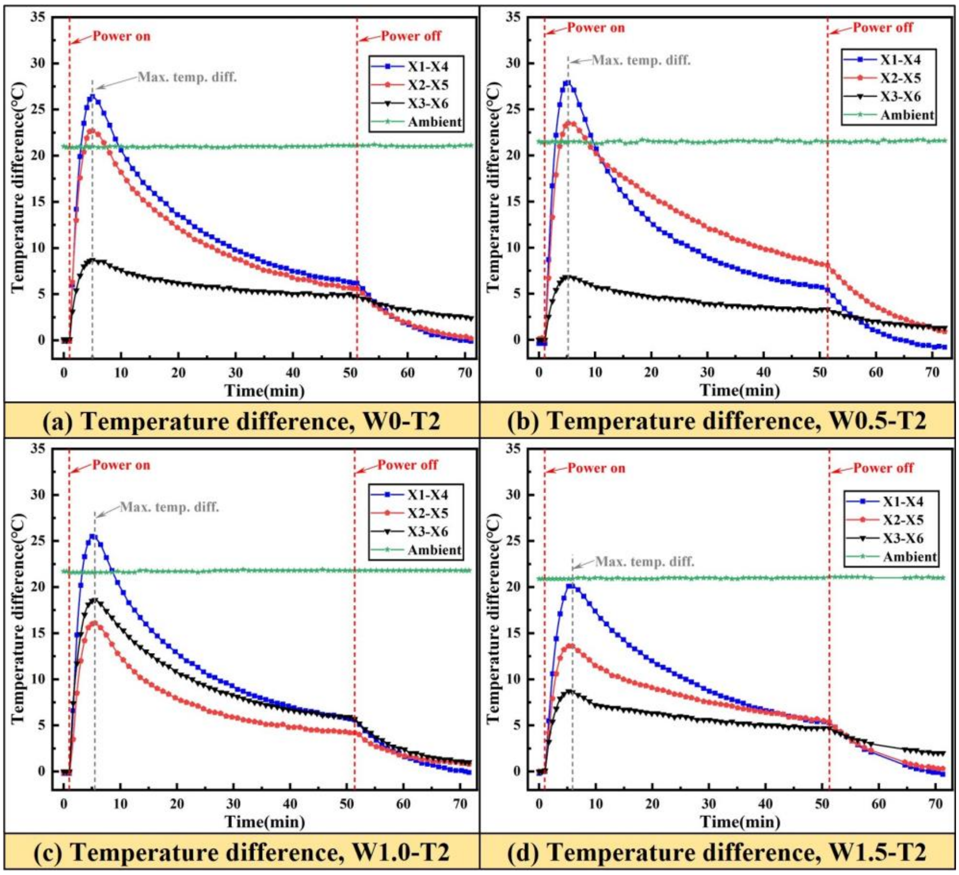

Fig. 9. Temperature differences of M1-T2.

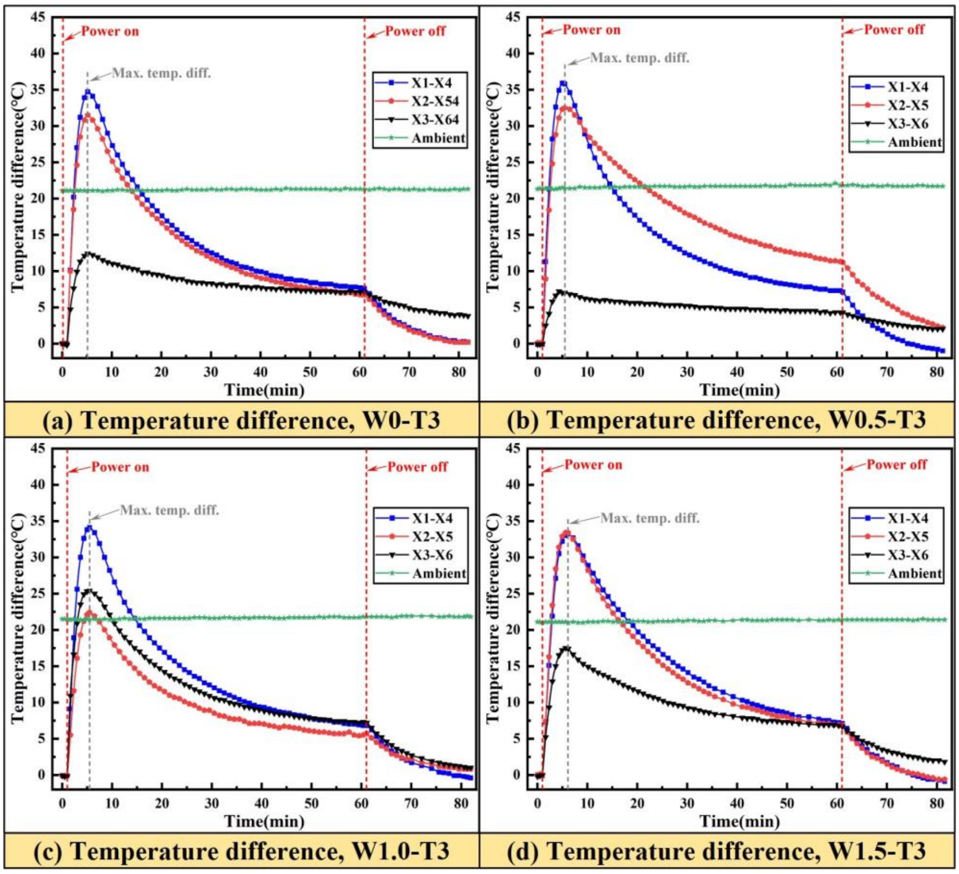

Fig. 10. Temperature differences of M1-T3.

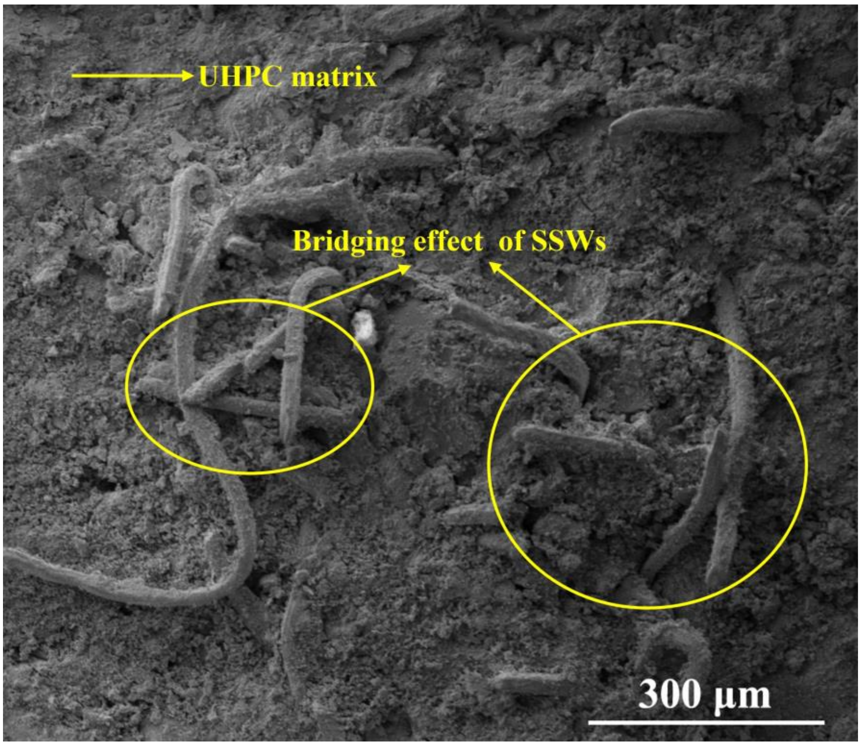

Fig. 11. SEM image of UHPC with 1.5 vol.% SSWs.

Figs. 12, 13 and 14 display the temperature strain histories of M1 experiments, in which the upper and lower parts of the X-axis, respectively, represent tensile and compressive strains. The absent data (Y2L of the W1.0 slab in Figs. 12 to 14) is caused by communicating cable failure. It can be vividly depicted in these figures that the strain curves show obvious hysteresis, implying that the changes in strain of the slabs are not immediately reflected when the temperature changes. Besides, the overall trend of strain is dominated by tensile strain, showing that the HS of the slab is stretched when being heated, and this phenomenon is consistent with the principles of thermal expansion. It is worth noting that although compressive strain occurs at some measuring points, most of them eventually exhibit a transition from compressive to tensile strains, as evidenced by the curves crossing the X-axis from negative to positive. The simultaneous occurrence of tensile and compressive strains can be attributed to the uneven deformation of the slabs. As the deformation rates of different parts are not equal, the areas with slower tensile deformation are squeezed into compressive strain by the areas with faster tensile deformation. The tensile/compressive strains of the W1.5 slab under T1, T2 and T3 are

83.1%/82.2%, 79.8%/84.1% and 82.6%/85.8% lower than that of the W0 slab. So it is obvious that when adding 1.5 vol.% of SSWs into the UHPC matrix, the strain is greatly lessened, thus confirming that the TDB self-moderate effect of the developed composite is rather good.

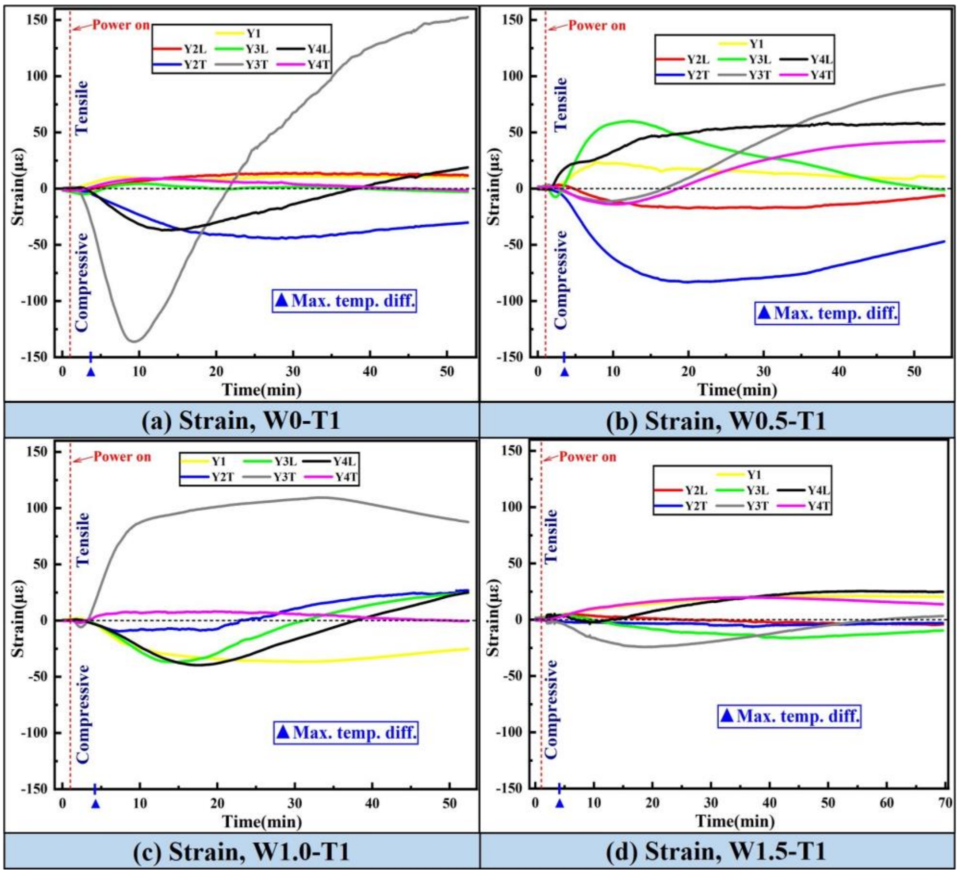

Fig. 12. Temperature strain histories of M1-T1.

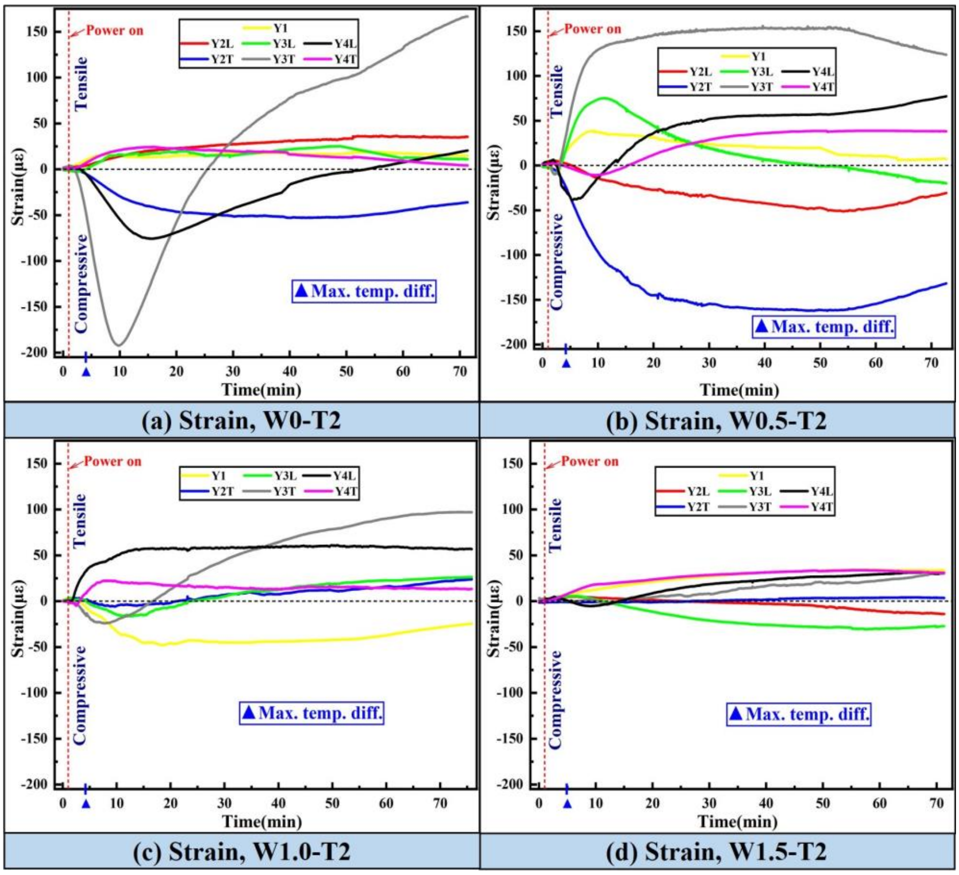

Fig. 13. Temperature strain histories of M1-T2.

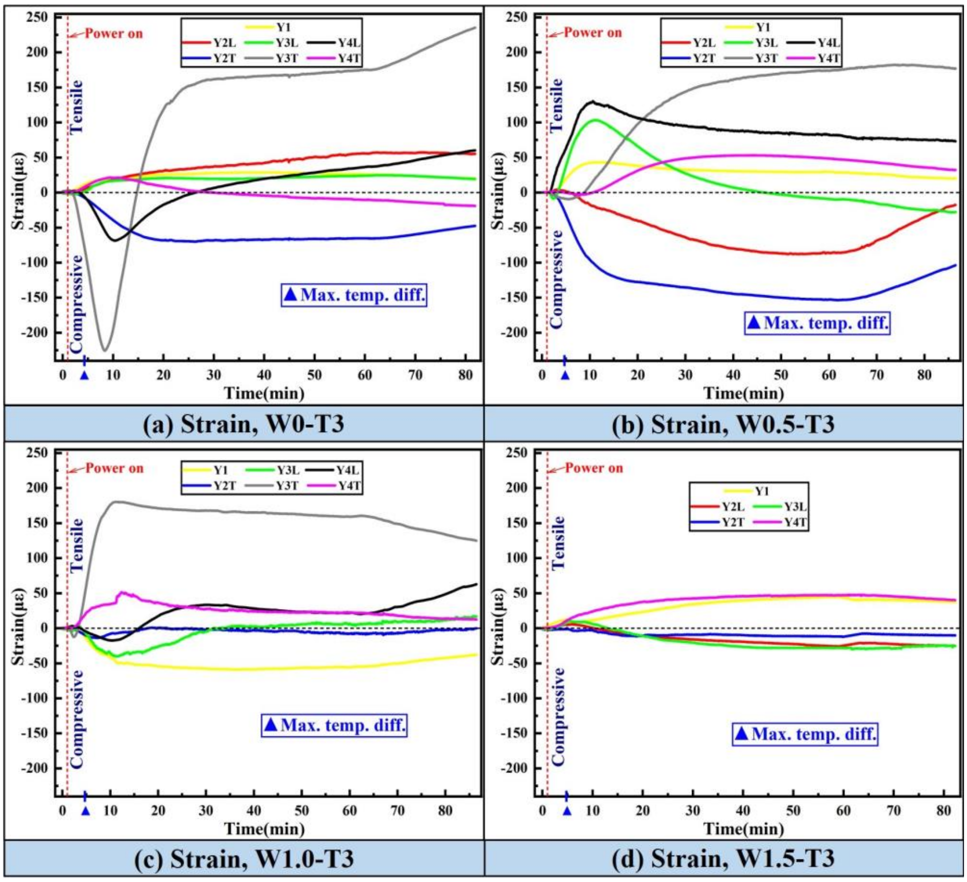

Fig. 14. Temperature strain histories of M1-T3.

When the slabs undergo temperature deformations, the values of the internal thermal stress are much smaller than their own flexural-tensile stresses [42], indicating that the temperature deformations are within the elastic range. Based on this assumption, the maximum strain can be calculated using the Eq. (7):

$$\sigma_{max}=\varepsilon_{max}\times E_s \tag{7}$$

where σ_{max} is the maximum stress of each slab, ε_{max} is the maximum strain of the slab, E_s is the elastic modulus of the slab.

Fig. 15 summarises the maximum temperature difference, extreme value of strain and maximum stress in M1 experiments. This figure clearly illustrates that the maximum temperature difference and extreme value of strain are, both, significantly optimised due to the incorporation of SSWs. Compared to the W0 slab, the W1.5 slab demonstrates a notable reduction in the maximum temperature difference and extreme value of strain by up to 32.1% and 85.6%, respectively. This evidence is sufficient to illustrate that a high content of SSWs can effectively enhance the thermal conductivity of the UHPC matrix, thus moderating the TDB of pavement slabs. At the target temperature of 80 °C, the W1.5 slab demonstrates a reduction of 76.8% in tensile stresses compared with the W0 slab, and the compressive stress can be restrained by 82.0% at a target temperature of 65 °C.

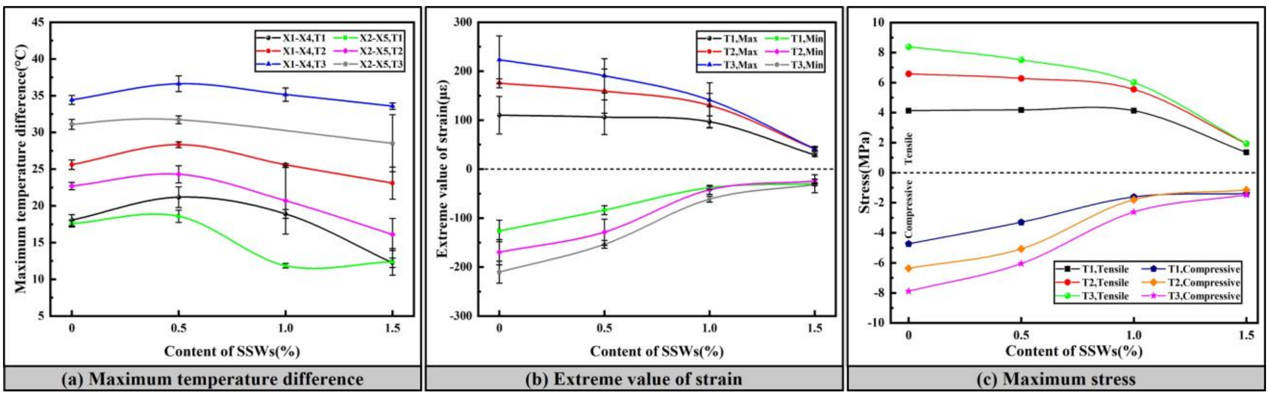

Fig. 15. Data outlines of M1 experiments.

A total of 48 M1 cyclic experiments are conducted, and all the results are listed in Table 3.

Table 3 Complete results of M1 cyclic experiments

Code names	Max. X (°C)	Max. +Y (με)	Min. -Y (με)	Code names	Max. X (°C)	Max. +Y (με)	Min. -Y (με)
W0T1K1	17.3	132.6	-124.3	W1.0T1K1	18.2	114.1	-40.0
W0T1K2	18.8	79.1	-96.5	W1.0T1K2	18.7	93.8	-33.8
W0T1K3	17.5	152.6	-136.2	W1.0T1K3	19.6	87.7	-36.6
W0T1K4	18.6	76.3	-148.1	W1.0T1K4	19.1	91.8	-41.4
W0T2K1	24.9	166.6	-191.2	W1.0T2K1	25.6	97.0	-48.8
W0T2K2	25.3	169.5	-157.7	W1.0T2K2	25.7	103.4	-47.7
W0T2K3	25.8	186.5	-139.2	W1.0T2K3	25.7	122.8	-43.6
W0T2K4	26.4	178.8	-190.9	W1.0T2K4	25.4	197.6	-28.9
W0T3K1	33.5	235.2	-197.0	W1.0T3K1	34.1	150.8	-66.8
W0T3K2	34.7	259.5	-225.0	W1.0T3K2	34.8	124.9	-53.9
W0T3K3	34.7	152.2	-233.2	W1.0T3K3	35.5	153.5	-59.1
W0T3K4	34.8	247.1	-186.0	W1.0T3K4	36.2	135.4	-66.1
W0.5T1K1	20.9	81.6	-93.5	W1.5T1K1	12.1	32.4	-13.2
W0.5T1K2	22.9	158.5	-86.7	W1.5T1K2	12.9	29.6	-25.3
W0.5T1K3	19.5	91.5	-71.5	W1.5T1K3	12.6	27.4	-55.9
W0.5T1K4	21.4	92.6	-83.2	W1.5T1K4	11.4	25.8	-24.2
W0.5T2K1	28.8	196.9	-95.9	W1.5T2K1	20.1	33.6	-30.4
W0.5T2K2	28.5	117.0	-127.7	W1.5T2K2	22.9	41.6	-21.6
W0.5T2K3	27.9	123.6	-161.4	W1.5T2K3	24.4	43.5	-23.4
W0.5T2K4	28.1	199.6	-130.0	W1.5T2K4	25.0	45.3	-22.5
W0.5T3K1	35.8	168.0	-143.7	W1.5T3K1	33.4	39.0	-30.6
W0.5T3K2	36.2	242.9	-154.7	W1.5T3K2	33.5	45.6	-33.9
W0.5T3K3	36.3	177.0	-163.1	W1.5T3K3	34.2	40.9	-31.9
W0.5T3K4	38.2	174.6	-152.8	W1.5T3K4	33.2	40.2	-29.7

3.1.2 Self-moderating performance under different heating rates

The M2 experiments are conducted to verify the results gained in M1 experiments, so instead of repeatedly displaying all results on temperature and strain, a brief presentation of key information is chosen in this part. Fig. 16 reflects the temperature difference and strain curves of M2 experiments. Since the infrared heating lamp possesses higher output power, its heating rate is much greater than that of the digital heating stage, so the curves of temperature difference are sharper than that of M1 experiments. Fig. 16 illustrates that the abrupt peaks in strains occur subsequent to those of temperature difference, a phenomenon explainable for two reasons. Firstly, when one side of the slab is heated, heat energy propagates through the thickness of the slab. As the temperature difference reaches the maximum value, heat transfer persists, leading to a time lag between temperature difference and strain. Secondly, temperature deformation is not an instantaneous process. As heat energy continues to build up, thermal stress gradually accumulates in the slab. When the temperature difference reaches a peak, the temperature deformation persists. These two main reasons collectively lead to this strain hysteresis phenomenon, which aligns with the results of M1 experiments. As the SSWs content increases from 0 to 1.5 vol.%, the maximum temperature difference, maximum strain and minimum strain are, respectively, moderated by 17.3%, 60.5% and 91.2%. The strain curves quickly approach 0 after sudden changes; this behaviour is attributed to the fact that the deformation caused by a short-term temperature change cannot last long, and the slabs can rapidly return to the original shape after deformation. Due to the uncovered HS, the temperature fluctuates during the experimental procedures, explaining the minor variations in temperature difference and strain as depicted in Fig. 16(b).

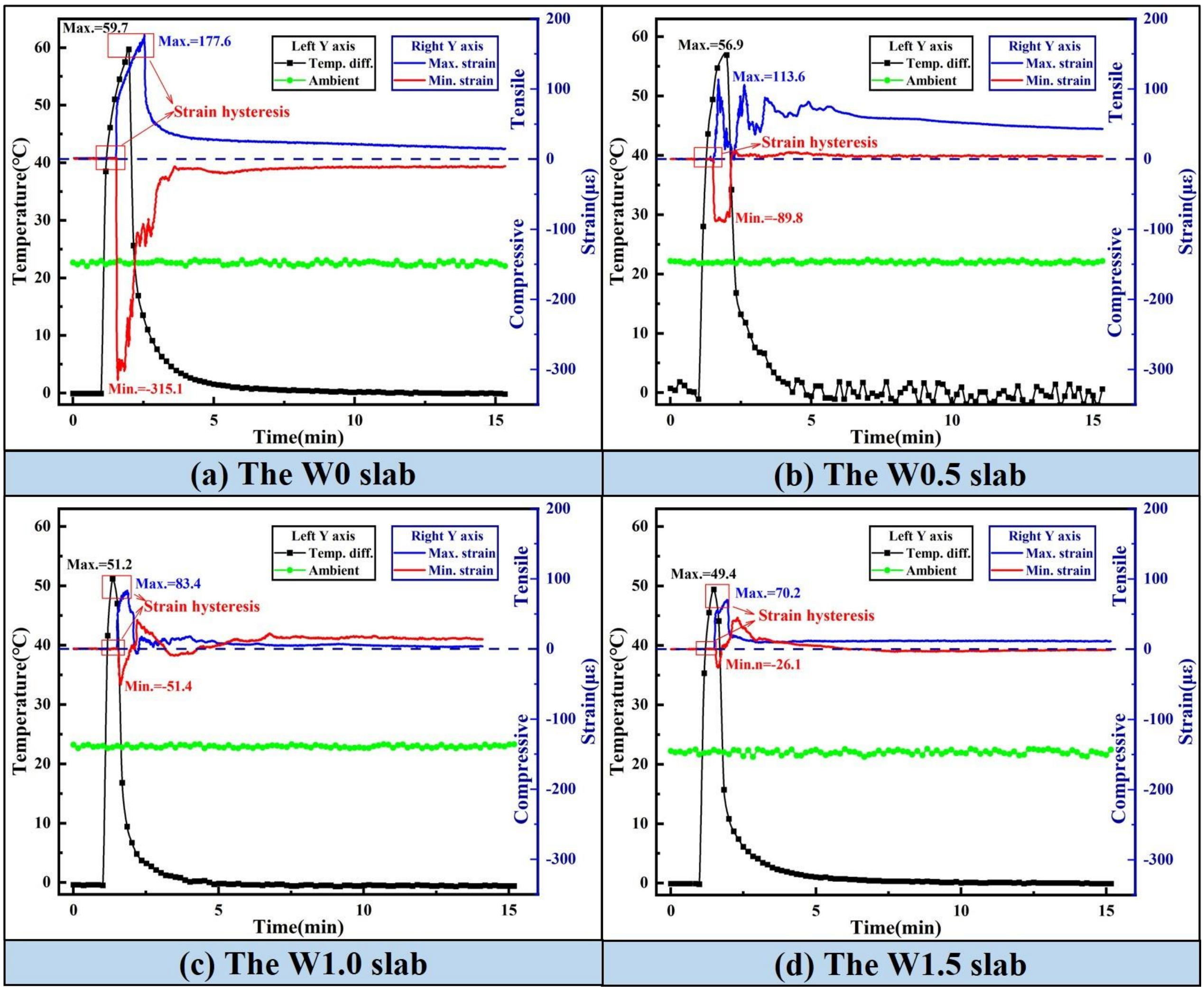

Fig. 16. Temperature difference and strain curves of M2 experiments.

Fig. 17 exhibits the vertical displacement of the slab corner (measuring point L) collected by LVDT under 3 target distances (i.e., 3 different heating rates). As the slabs curl downward when being heated, the slab corners move down. In this circumstance, the greater the vertical displacement is, the more significant the deformation would be. In the image, it is particularly obvious that the vertical displacement of the W0 slab is much larger than that of any SSWs-incorporated slabs. Similar to strain curves, the vertical displacement curves also tend to stabilise after brief changes. As shown in Fig. 17(a), the heating rate of D1 is much higher than that of D2 and D3, so the time of Fig. 17(b) and Fig. 17(c) has been remarkably prolonged, thus the W0.5 and W1.0 slabs stabilise far above 0. The vertical displacements of the W1.5 slab are as tiny as almost undetectable in the experiments, measuring 0.0015 mm at a heating rate of 67.1 °C/min, 0.0008 mm at a heating rate of 20.1 °C/min and 0.0752 mm at a heating rate of 11.0 °C/min, respectively. Compared with that of the W0 slab, deflections of the W1.5 slab have decreased by 98.6%, 99.4% and 73.2%, for the respective heating rates mentioned above.

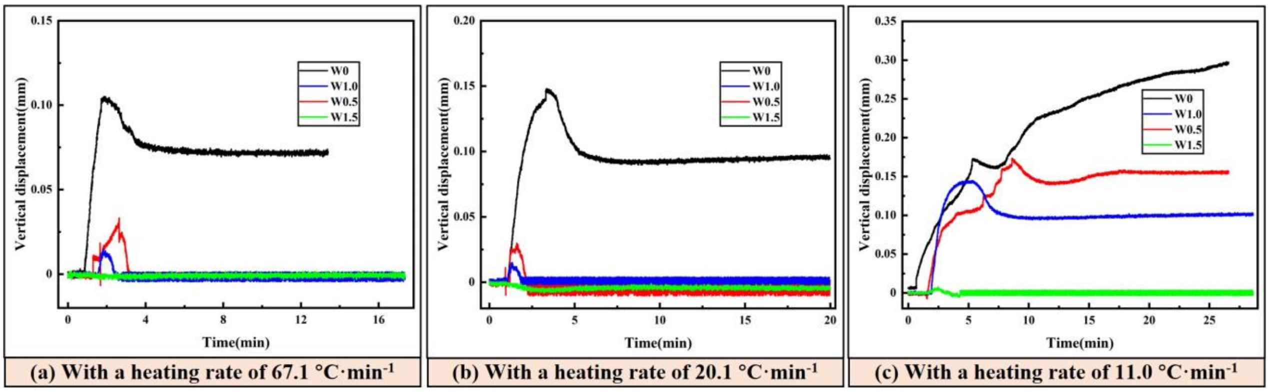

Fig. 17. Vertical displacement of M2 experiments.

Fig. 18 outlines the tendency of the maximum temperature difference, maximum vertical displacement, extreme value of strain and maximum stress of M2 experiments. Similar to the M1 experiments, adding only 0.5 vol.% of SSWs is not adequate to significantly reduce the temperature difference, but is sufficient to moderate strain and vertical displacement. The high content of SSWs (1.5 vol.%) demonstrates momentous effects on suppressing the negative development of temperature differences, vertical displacements, strains and stresses. In contrast to the W0 slab, the slab containing 1.5 vol.% of SSWs demonstrates a reduction of 66.0% in tensile stresses at a heating rate of 11.0 °C/min and a decrease of 89.6% in compressive stresses at a heating rate of 67.1 °C/min.

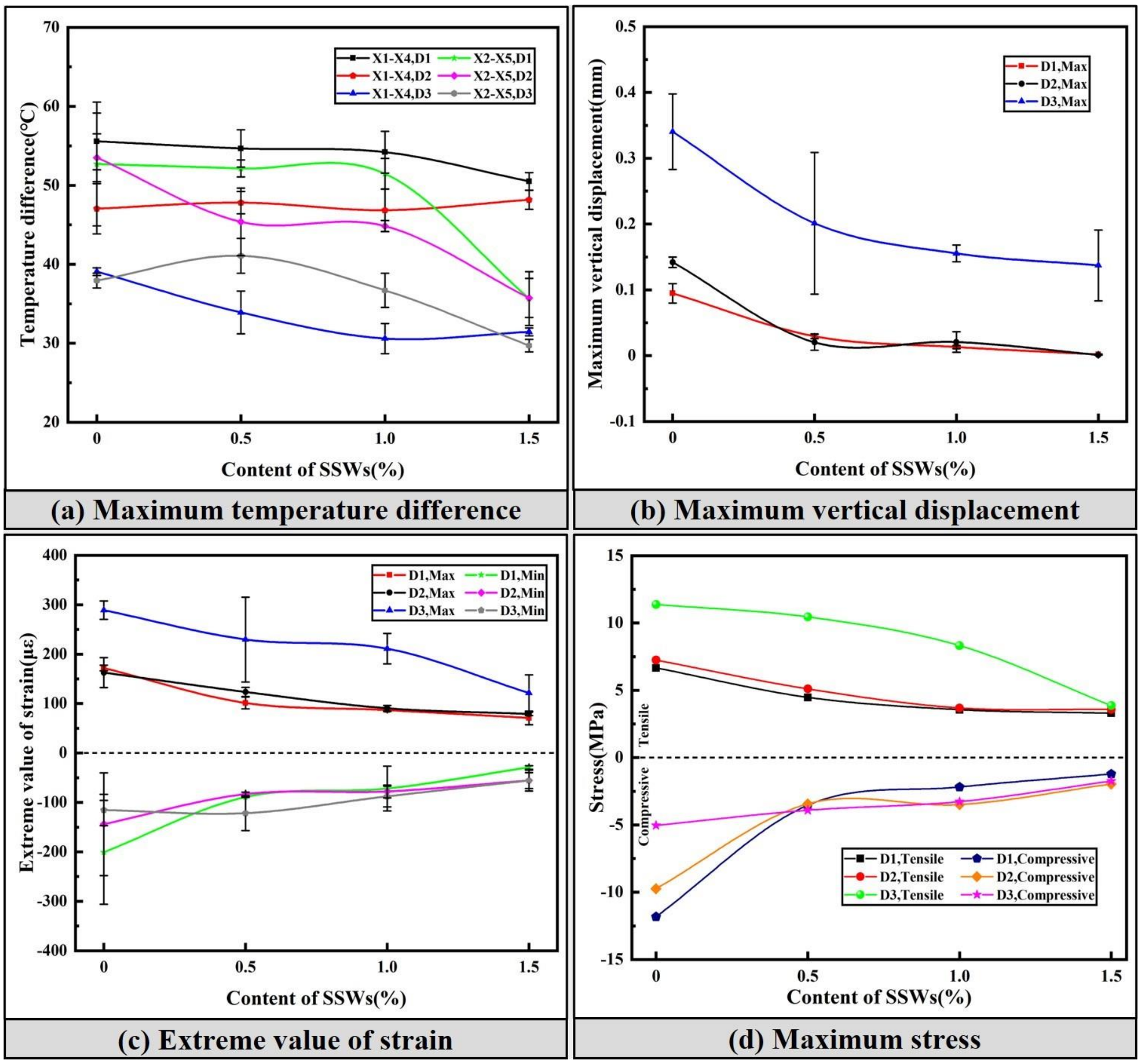

Fig. 18. Tendency outlines of M2 experiments.

A total of 36 M2 cyclic experiments have been conducted, and the full data can be viewed in Table 4 below.

Table 4 Complete results of M1 cyclic experiments

Code names	Max. X(°C)	Max. +Y(με)	Min. -Y (με)	Max. L(mm)	Code names	Max. X(°C)	Max. +Y(με)	Min. -Y (με)	Max. L(mm)
W0D1K1	53.1	166.3	-108.8	0.1051	W1.0D1K1	51.2	89.2	-51.4	0.0105
W0D1K2	53.9	171.6	-178.5	0.0842	W1.0D1K2	56.2	83.4	-40.5	0.0150
W0D1K3	59.7	177.6	-315.1	/	W1.0D1K3	55.2	87.8	-123.7	0.0137
W0D2K1	43.6	162.0	-58.5	0.1482	W1.0D2K1	46.1	96.7	-87.9	0.0086
W0D2K2	49.9	193.2	-259.6	0.1448	W1.0D2K2	44.6	86.5	-82.1	0.0151
W0D2K3	47.6	132.4	-114.1	0.1330	W1.0D2K3	49.8	87.6	-63.2	0.0383
W0D3K1	31.2	268.2	-133.1	0.3808	W1.0D3K1	23.1	246.4	-112.0	0.1687
W0D3K2	31.1	303.4	-79.0	/	W1.0D3K2	25.0	195.3	-74.7	0.1435
W0D3K3	32.0	295.1	-134.4	0.2997	W1.0D3K3	43.7	191.1	-76.9	0.1541
W0.5D1K1	54.9	100.2	-88.6	0.0262	W1.5D1K1	50.5	70.2	-33.0	0.0015

W0.5D1K2	52.2	113.6	-89.3	0.0287	W1.5D1K2	51.6	85.2	-26.1	0.0021
W0.5D1K3	56.9	89.6	-89.8	0.0332	W1.5D1K3	49.4	57.3	-28.9	0.0022
W0.5D2K1	47.6	112.6	-87.3	0.0242	W1.5D2K1	46.9	76.2	-42.0	0.0008
W0.5D2K2	49.3	128.4	-79.3	0.0067	W1.5D2K2	49.3	82.8	-45.0	0.0008
W0.5D2K3	46.5	129.4	-83.2	0.0299	W1.5D2K3	48.3	78.3	-80.1	0.0015
W0.5D3K1	38.9	131.4	-99.4	0.0853	W1.5D3K1	32.6	126.0	-66.2	0.0752
W0.5D3K2	39.6	265.2	-162.6	0.2202	W1.5D3K2	32.1	155.7	-37.3	0.1652
W0.5D3K3	38.7	291.7	-103.3	0.2980	W1.5D3K3	37.0	82.4	-63.7	0.1714

3.1.3 Self-moderating performance in the outdoor environment

Due to the limitations of testing channels, the M3 experiments are carried out over 2 consecutive days. On the first day, the W0 and W1.5 slabs are tested together while the measurements are taken for the W0.5 and W1.0 slabs on the following day. Fig. 19 portrays the temperature and wind speed of M3 experiments, and it is graphically depicted that the temperatures on the HS are fluctuating due to the influence of wind speed (values up to 1.7 m/s). The maximum temperatures and slopes of the curves are not equal because the wind speed and weather conditions were not exactly the same in the 2 days of testing. Due to the slow heating rate of sunlight exposure and high ambient temperature, the initial temperatures of UnHS are higher than M1 and M2 experiments while the temperature differences are much lower. As for the 2 slabs that are tested on the same day, the one with high SSWs content has denser temperature curves, meaning the temperature differences are lower.

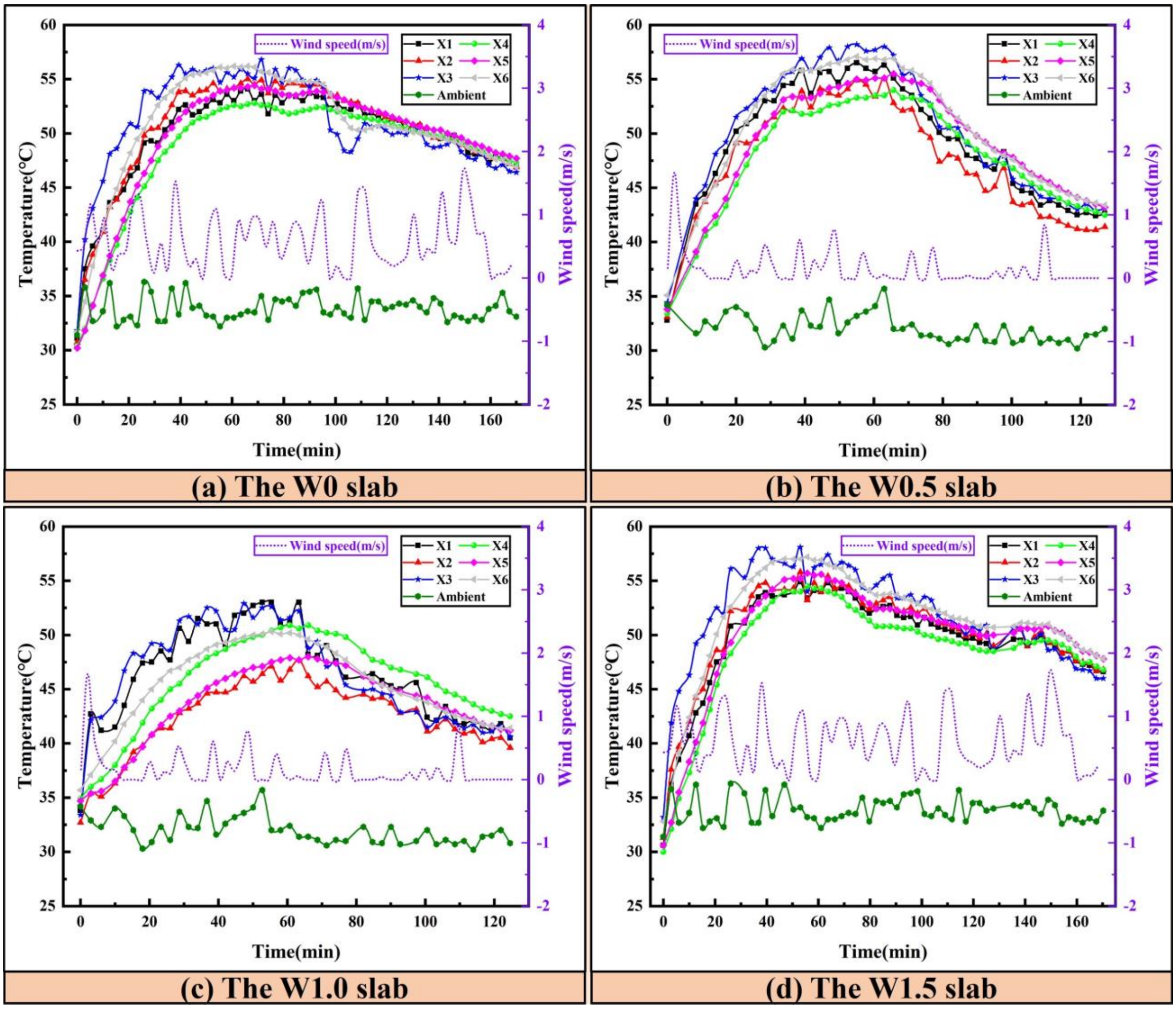

Fig. 19. Temperature and wind speed of M3 experiments.

Fig. 20 delineates the temperature differences of M3 experiments. In the figure, the curves distinctly exhibit two stages: above 0 °C and below 0 °C. Firstly, the slabs are exposed to sunlight, and the temperatures on HS continue to rise, so the temperature differences are greater than 0 °C. Then as heat energy is transferred through the thickness direction, the temperatures on UnHS develop. The heat energy of HS is dissipated faster under the influence of wind, while the heat energy of HnHS is dissipated more slowly due to the presence of EPE foam, resulting in negative temperature differences in M3 experiments. Compared with that of the W0 slab, the positive temperature difference of the W1.5 slab decreases by 12.3%, and the negative temperature difference is moderated by 25.0%.

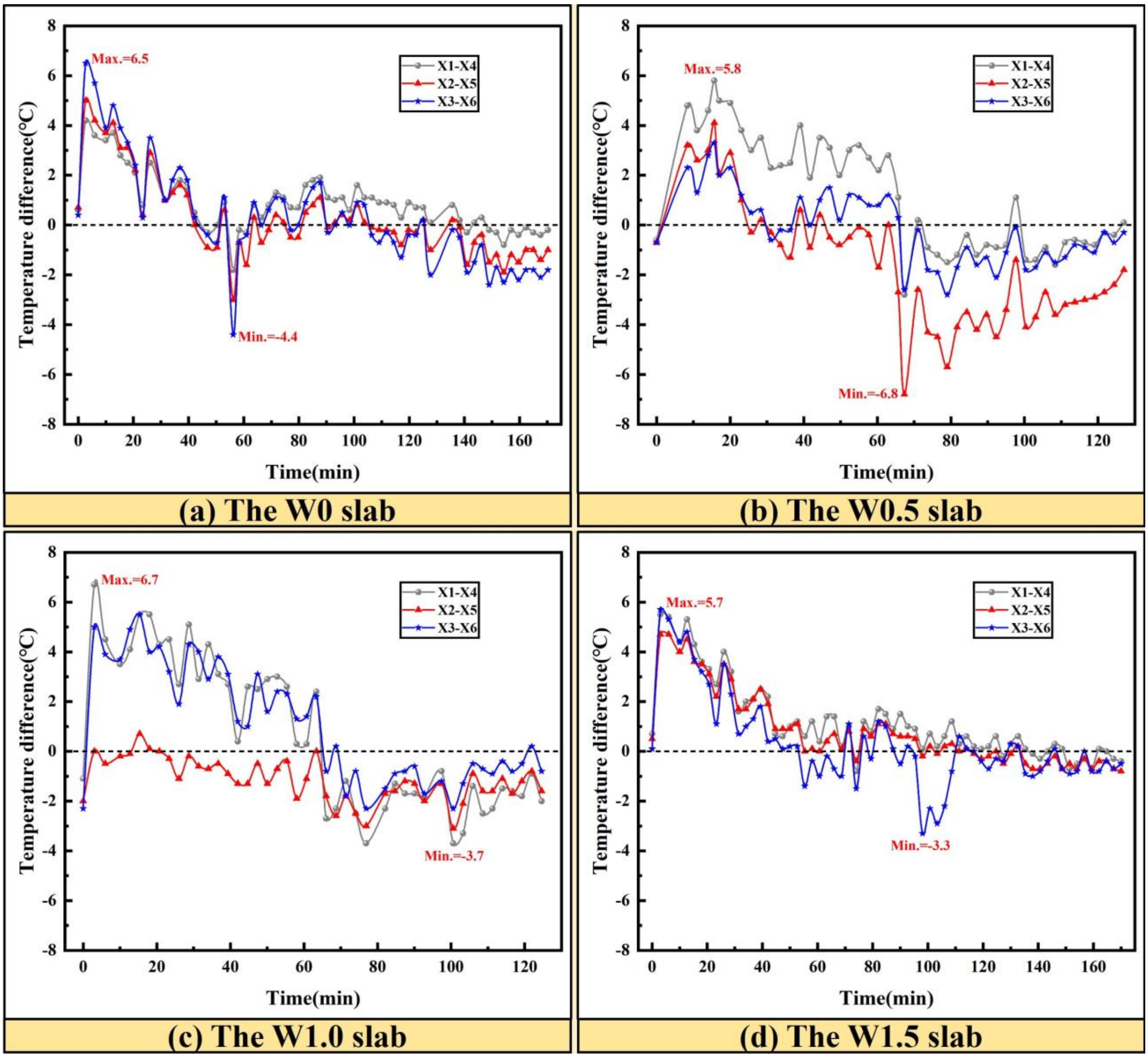

Fig. 20. Temperature difference of M3 experiments.

Fig. 21 illustrates the strain curves of M3 experiments. The prominent feature is the oscillating nature of the strain curves, caused by outdoor wind. The maximum strains of the W0 and W1.5 slabs are 220.7 με and 51.7 με, demonstrating a significant drop of 76.6%. On the other hand, the maximum strains of the W0.5 and W1.0 slabs are 159.0 με and 125.6 με, a decrease of 21.0%. The negative strains have been self-moderated by 21.0% and 14.9% when making the same comparison. Affected by different ambient temperatures and sunlight intensity, the deformation trends are different among the 4 slabs. The strains of W0.5 and W1.0 slabs are dominated by tensile strains while those of the W0 and W1.5 slabs don’t show this specific trend.

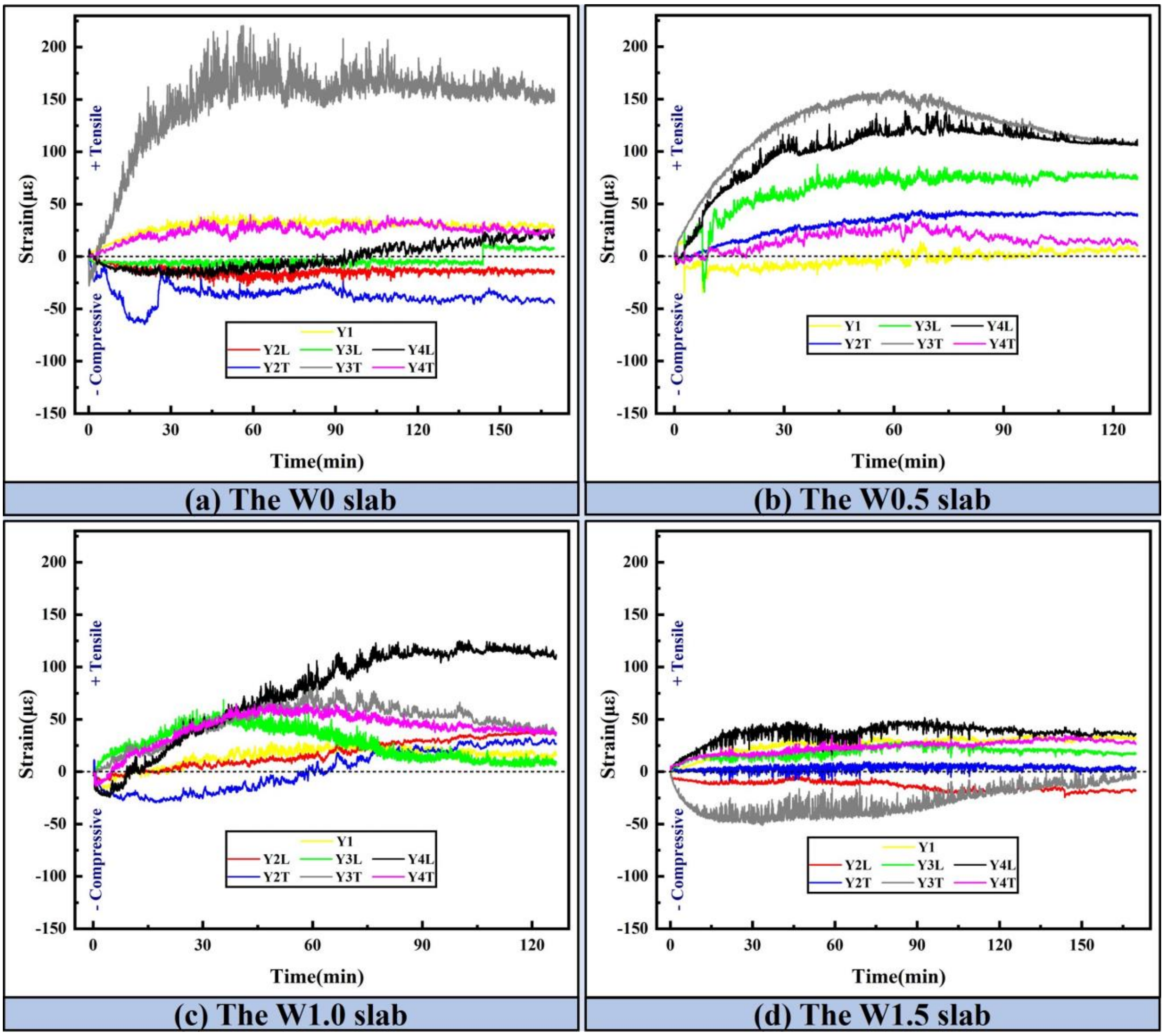

Fig. 21. Strain curves of M3 experiments.

In order to further prove the reducing effect of SSWs on temperature difference and eliminate the impact of different weather conditions, the 4 slabs are tested together in the sunlight, and the results are illustrated in Fig. 22. The measuring points X1 and X4 of each slab are employed to represent the temperatures of HS and UnHS, and the maximum wind speed is 1.9 m/s. From this image, it can be drawn out that the W1.5 slab is the most effective in diminishing the temperature difference, although its surface temperatures are not the lowest in the entire process. In comparison to the unreinforced UHPC slab, the SSWs enhanced UHPC slabs exhibit a reduction in the tensile stress by 48.1% (1.0 vol.%) and a decrease in the compressive stress by 70.7% (1.5 vol.%).

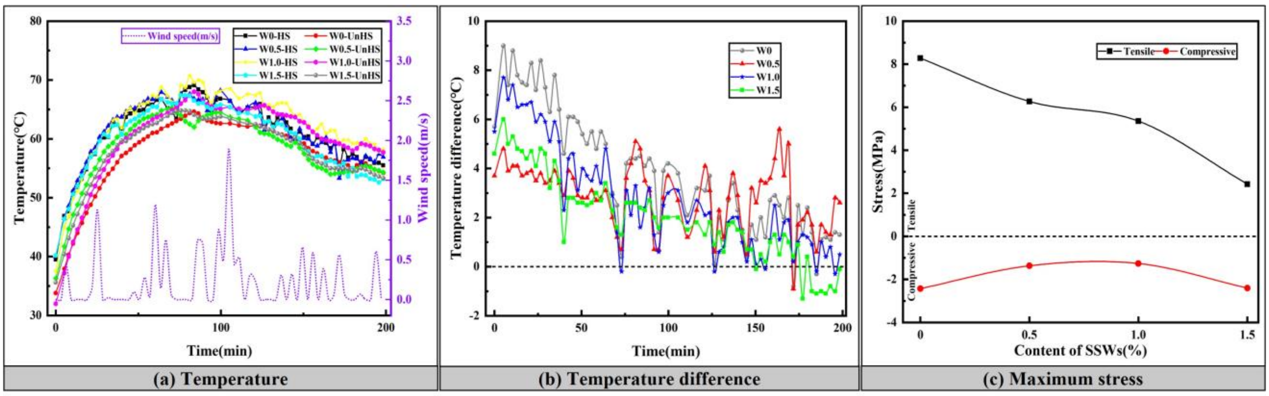

Fig. 22. Temperature, temperature difference and stress in outdoor experiments.

3.2 TDB self-sensing performance

Incorporating SSWs into the UHPC matrix has the dual benefit of not only improving the thermal conductivity of the composites but also enhancing their electrical conductivity. The self-sensing of TDB is accomplished by detecting the changes in the resistance of the slabs. The TDB self-sensing experiments are exclusively conducted on the W0.5, W1.0 and W1.5 slabs, as the W0 slab without SSWs demonstrates poor electrical conductivity. Prior to each self-sensing experiment (S experiment), the slab is connected to the resistance-collecting equipment for 30 minutes in order to achieve polarization, and data collected during this polarization period are not shown in this part.

Fig. 23 illustrates the relationship between resistance changes and temperature differences, including resistance and *FCR*. The missing curve of X2-X5 in Fig. 23(c) is a result of technical glitches encountered during the measurement of that particular channel. As concluded in the former sections, the temperature difference declines when SSWs content increases. The maximum temperature differences of the W0.5, W1.0 and W1.5 slabs are recorded as 48.5 °C, 44.6 °C and 35.5 °C, respectively, exhibiting a drop of 8.0% and 26.8%, respectively, for the latter two in comparison with the W0.5 slab. Remarkably, the resistances of the three slabs frequently fluctuate within a minor range, and this fluctuation lasts until the temperature difference is small enough. After fluctuation, the resistance of the slabs returns to a relatively stable state. Meanwhile, the *FCR* of the three slabs significantly changes when being heated, and the response time is as short as 0.23 s. By monitoring these frequent and minor fluctuations of resistance, the TDB self-sensing can be realised with fairly low cost and non-carbon emission [50]. There are two underlying mechanisms that work together to enable the SSWs reinforced UHPC with TDB self-sensing capability. Firstly, when the UHPC slabs with SSWs are heated up, they tend to curl upward due to temperature difference, leading to minor changes in the internal electrically conductive network, thus affecting their resistivities. Secondly, based on the Seebeck effect [51], when one side of the slab is heated, a potential difference occur on both sides due to the temperature difference. This tiny potential difference acts on the resistivity measurement loop and cause frequent fluctuations in resistance in a small range. The combination of the above two reasons contributes to the phenomenon shown in Fig. 23.

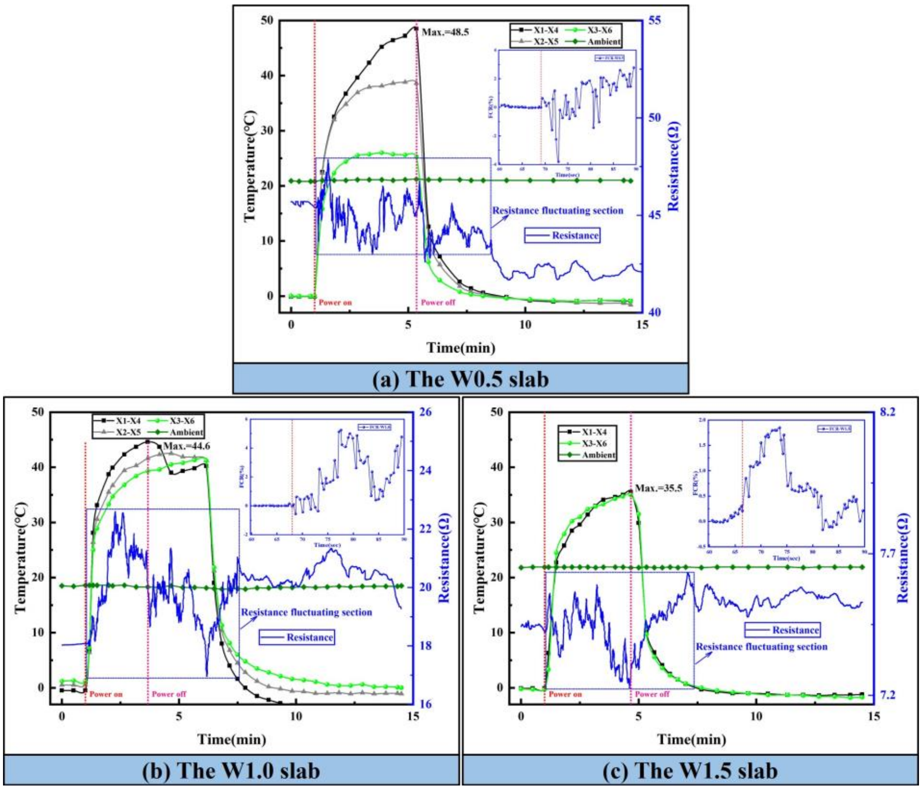

Fig. 23. Relationship between resistance changes and temperature differences.

Fig. 24 presents some evidence of TDB self-moderating and self-sensing gained in S experiments.

In which, Fig. 24(a) gives the resistivity of the slabs with different contents of SSWs, calculated using Eq. (8).

$$\rho=\frac{RS}{L} \tag{8}$$

where ρ is the resistivity of the slab (Ω·cm), R is the resistance of the slab (Ω, measured), S is the cross-sectional area size (~40 cm^2) of the slab, and L is the distance between the copper foil tapes (~ 20.5 cm).

Fig. 24(a) clearly shows that the electrical resistivities of the W1.0 slab and the W1.5 slab have, respectively, decreased by 51.7% and 81.7%, in comparison to the W0.5 slab, conclusively confirming that the incorporation of SSWs can simultaneously boost the thermal and electrical conductivity of the pavement slab.

The index called fractional changes in resistivity (*FCR*) is often used to characterise the self-sensing sensitivity of a composite and it can be calculated by the following Eq. (9):

$$FCR=\frac{\rho_i}{\rho_0} \tag{9}$$

where ρ_i and ρ_0 are the resistivity at a certain time point and the initial resistivity, respectively (unit: Ω·cm).

Fig. 24(b) justifies again that adding SSWs into the UHPC matrix is an adequate amount to minimise the temperature difference, and Fig. 24(c) determines that the developed UHPC can maintain a rather stable resistivity after being heated several times. The coefficient of variation (*CV*) serves as a statistical dimensionless index used to quantify the dispersion degree of data. A large value of CV indicates a high dispersion degree of experimental data. In this study, it is used to characterize the repeatability of self-sensing experiments and the long-term stability of the self-sensing performance. The calculation method for CV is presented in Eq. (10) [52]:

$$CV=\frac{\sigma_r}{\rho_a} \tag{10}$$

where σ_r is the standard deviation of resistivity while ρ_a is the average value of resistivity (Ω·cm).

Consequently, the results calculated from Eq. (10) are $CV_{0.5}$=6.0%, $CV_{1.0}$=7.8% and $CV_{1.5}$=3.2%, respectively. Normally, experimental repeatability is considered consistent if the CV value does not exceed 10%. Therefore, it is evident that the SSWs enhanced UHPC shows good resistivity stability after long-term service.

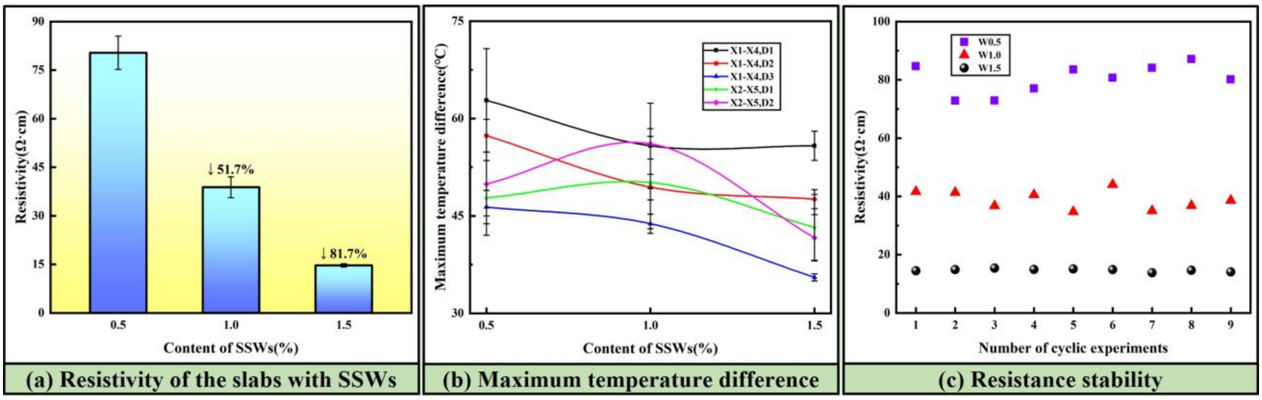

Fig. 24. Resistivity of slabs, maximum temperature difference and resistance stability in S experiments.

4. Conclusions

In this paper, the self-moderating and self-sensing capabilities for temperature deformation behaviour of UHPC with SSWs were fully investigated. Subsequently, the presentation of temperature difference and strain data was employed to demonstrate the self-moderating and self-sensing performances of SSWs enhanced UHPC. Lastly, the coefficient of variation was calculated to verify that such composite can maintain stable self-moderating and self-sensing performances after long-term service. The major conclusions of this study are listed below.

1) In the indoor environment, the surface temperatures of the slabs develop in two nonlinear stages with the heating rate decreasing, and the maximum temperature difference appears at the transition point between the two stages. The heating rate accelerates with the increase of SSWs content, while

the temperature difference drops. Compared with the W0 slab, the W1.5 slab reduces 39.4% of temperature difference, 83.1%/82.2% of tensile/compressive strains when the target temperature is 50 °C according to the results of 48 cyclic experiments with the digital heating stage.

2) The strains in the slabs have a significant hysteresis effect, and the time of hysteresis is about 0.53 min. The vertical displacement sharply increases upon initiation of heating, subsequently approaching 0. The vertical displacement of W1.5 slab is 99.4% lower than that of the W0 slab when the heating rate is 20.1 °C/min. According to the results of 36 sourced cyclic experiments with the infrared heating lamp, the increase of SSWs content from 0 to 1.5 vol.% correlates with a reduction in the maximum temperature differences by 17.3%, maximum tensile/compressive strains by 60.5%/91.2% and maximum tensile/compressive stresses by 66.0%/89.6%.

3) Compared with the W0 slab, the W1.5 slab reduces the positive/negative temperature differences by 12.3%/25.0% respectively, and the strain is also suppressed by 76.6% in the outdoor environment, unaffected by wind and solar radiation. The tensile/compressive stresses of the SSWs enhanced slabs have been restrained by 48.1%/70.7% than that of the unenhanced slab.

4) The resistances of SSWs reinforced slabs fluctuate in small scales when being heated, persisting until the temperature differences are very small. Meanwhile, the time of self-sensing response is as short as 0.23 s. The fractional changes in resistivity of the W1.0 slab can exceed 5%, and the coefficient of variation of the W1.5 slab is 3.2%, presenting outstanding self-sensing sensitivity and repeatability. Such composite maintains stable resistivity and sensitive self-sensing capability after being heated 27 times.

Consequently, the developed UHPC with SSWs possesses outstanding thermal conductivity as well as stable and precise temperature-change sensitivity, thereby enabling the engineering infrastructures with self-moderating and self-sensing capabilities on temperature deformations in scorching weather. Meanwhile, the performance of the developed composite is hardly influenced by the size effect as the SSWs bridge each other to form an extensive thermally conductive network. Combined with its stainless feature, outstanding durability and high toughness, SSWs can lessen the expenses during the whole service life. Therefore, the SSWs enhanced UHPC engineering infrastructures are characterised by distinctive features of minimal carbon emissions and multi-functionality. This configuration empowers real-time monitoring and timely maintenance throughout the entire life cycle of engineering infrastructures, enabling it as a promising composite for self-moderating and self-sensing the temperature deformations of engineering infrastructures, as referred to in Fig. 25.

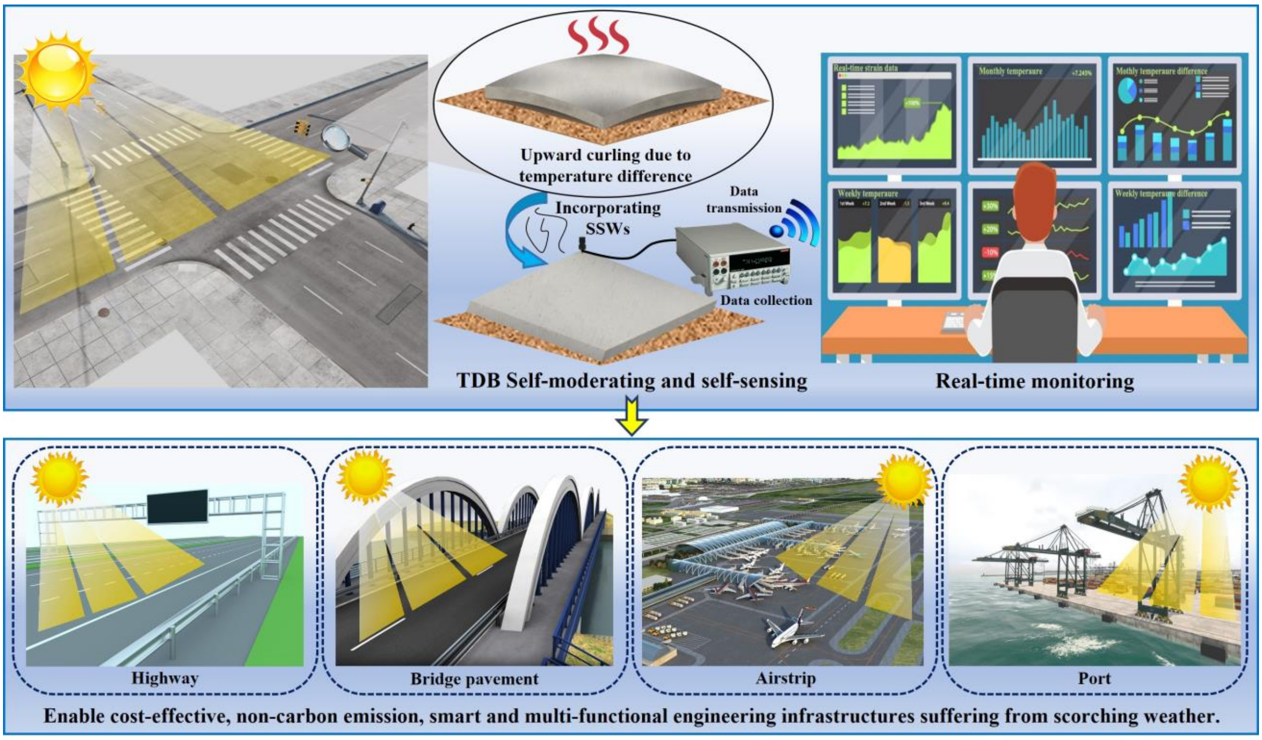

Fig. 25. Application prospects of SSWs reinforced UHPC.

Acknowledgments

The authors thank the funding supported from the National Science Foundation of China (Grant Nos. 51908103, 51978127, and 52178188), and the Major Science and Technology Research Project of the China Building Materials Federation (2023J BGS10-02).

References

[1] N.P. Sharifi, K.C. Mahboub, Application of a PCM-rich concrete overlay to control thermal induced curling stresses in concrete pavements, Construction and Building Materials. 183 (2018) 502-512.

[2] B. Han, L. Zhang, J. Ou, Smart and Multifunctional Concrete toward Sustainable Infrastructures, Springer, 2017.

[3] W. Du, C. Qian, Y. Xu, M. Wei, B. Peng, Y. Xie, Effects of ambient temperature, formwork type, and demolding time on the thermal deformation of sidewall concrete in underground engineering: Experiment, simulation, and engineering practice, Construction and Building Materials. 353 (2022) 129083.

[4] R. Jaafri, H. Samouh, E. Roziere, S.Y. Alam, V. Wisniewski, A. Loukili, Experimental and numerical analysis of curling behavior of natural hydraulic lime - cement based mortars, Cement and Concrete Research. 117 (2019) 1-15.

[5] Y. Zhong, L. Gao, Y. Zhang, Effect of daily changing temperature on the curling behavior and interface stress of slab track in construction stage, Construction and Building Materials. 185 (2018) 638-647.

[6] I. Papayianni, T. Valliasis, Heat deformations of fly ash concrete, Cement and Concrete Composites. 27 (2) (2005) 249-254.

[7] S. Ding, S. Dong, X. Wang, S. Ding, B. Han, J. Ou, Self-heating ultra-high performance concrete with stainless steel wires for active deicing and snow-melting of transportation infrastructures, Cement and Concrete Composites. 138 (2023) 105005.

[8] Q. Li, M. Wang, H. Sun, G. Yu, Effect of heating rate on the free expansion deformation of concrete during the heating process, Journal of Building Engineering. 34 (2021) 101896.

[9] K. Kim, S. Chun, B. Park, S. Han, Precast prestressed concrete pavement (PPCP): Effect of thermal gradient on curling deflection and stress, Construction and Building Materials. 274 (2021) 121966.

[10] J. Bosnjak, J. Ozbolt, R. Hahn, Permeability measurement on high strength concrete without and with polypropylene fibers at elevated temperatures using a new test setup, Cement and Concrete Research. 53 (2013) 104-111.

[11] S. Dong, X. Wang, B. Han, Stainless Steel Wires-Engineered Multifunctional Ultra-High Performance Concrete, Taylor & Francis, 2023.

[12] W. Liao, C. Zeng, Y. Zhuang, H. Ma, W. Deng, J. Huang, Mitigation of thermal curling of concrete slab using phase change material: A feasibility study, Cement and Concrete Composites. 120 (2021) 104021.

[13] G. Wang, Z. Tang, Y. Gao, P. Liu, Y. Li, A. Li, X. Chen, Phase change thermal storage materials for interdisciplinary applications, Chemical Reviews. 123 (11) (2023) 6953-7024.

[14] M. Belshe, M.S. Mamlouk, K.E. Kaloush, M. Rodezno, Temperature gradient and curling stresses in concrete pavement with and without open-graded friction course, Journal of Transportation Engineering. 137 (10) (2011) 723-729.

[15] A.E. Canga Ruiz, Y. Qian, J.R. Edwards, M.S. Dersch, Analysis of the temperature effect on concrete crosstie flexural behavior, Construction and Building Materials. 196 (2019) 362-374.

[16] S.R. Kasu, S. Patel, A.R. Muppireddy, Field experiments and numerical analysis of curling behavior of cast-in-situ short paneled concrete pavement on lean concrete base, The International Journal of Pavement Engineering. 23 (11) (2022) 3743-3756.

[17] H. Zhu, Q. Li, Y. Hu, Self-developed testing system for determining the temperature behavior of concrete, Materials. 10 (4) (2017) 419.

[18] M. Azenha, R. Faria, D. Ferreira, Identification of early-age concrete temperatures and strains: Monitoring and numerical simulation, Cement and Concrete Composites. 31 (6) (2009) 369-378.

[19] W. Liao, Y. Zhuang, C. Zeng, W. Deng, J. Huang, H. Ma, Fiber optic sensors enabled monitoring of thermal curling of concrete pavement slab: Temperature, strain and inclination, Measurement. 165 (2020) 108203.

[20] B. Han, S. Ding, J. Wang, J. Ou, Nano-Engineered Cementitious Composites: Principles and Practices, Springer, 2019.

[21] L.M. Seymour, J. Maragh, P. Sabatini, M. Di Tommaso, J.C. Weaver, A. Masic, Hot mixing: Mechanistic insights into the durability of ancient Roman concrete, Science Advances. 9 (1) (2023).

[22] S. Ding, X. Wang, B. Han, New-Generation Cement-Based Nanocomposites, Springer, 2023.

[23] M. Papachristoforou, E.K. Anastasiou, I. Papayianni, Durability of steel fiber reinforced concrete with coarse steel slag aggregates including performance at elevated temperatures, Construction and Building Materials. 262 (2020).

[24] Z.C. Huang, J. Ho, J. Cui, F.M. Ren, X. Cheng, M.H. Lai, Improving the post-fire behaviour of steel slag coarse aggregate concrete by adding GGBFS, Journal of Building Engineering. 76 (2023).

[25] J.H. Han, D.B. Wang, P. Zhang, Effect of nano and micro conductive materials on conductive properties of carbon fiber reinforced concrete, Nanotechnology Reviews. 9 (1) (2020) 445-454.

[26] S. Gwon, H. Kim, M. Shin, Self-heating characteristics of electrically conductive cement composites with carbon black and carbon fiber, Cement and Concrete Composites. 137 (2023).

[27] H.W. Iqbal, R.A. Khushnood, W.L. Baloch, A. Nawaz, R.F. Tufail, Influence of graphite nano/micro platelets on the residual performance of high strength concrete exposed to elevated temperature, Construction and Building Materials. 253 (2020).

[28] T. Wu, R. Huang, M. Chi, T. Weng, A study on electrical and thermal properties of conductive concrete, Computers and Concrete. 12 (3) (2013) 337-349.

[29] D. Lu, L.P. Ma, J. Zhong, J.M. Tong, Z.B. Liu, W.C. Ren, H.M. Cheng, Growing nanocrystalline graphene on aggregates for conductive and strong smart cement composites, ACS Nano. 17 (4) (2023) 3587-3597.

[30] D.X. Luong, K.V. Bets, W.A. Algozeeb, M.G. Stanford, C. Kittrell, W. Chen, R.V. Salvatierra, M.Q. Ren, E.A. McHugh, P.A. Advincula, Z. Wang, M. Bhatt, H. Guo, V. Mancevski, R. Shahsavari, B.I. Yakobson, J.M. Tour, Gram-scale bottom-up flash graphene synthesis, Nature. 577 (7792) (2020) 647-651.

[31] S.J. Lee, I. You, S. Kim, H.O. Shin, D.Y. Yoo, Self-sensing capacity of ultra-high-performance fiber-reinforced concrete containing conductive powders in tension, Cement and Concrete Composites. 125 (2022).

[32] M. Gastaldi, L. Bertolini, Effect of temperature on the corrosion behaviour of low-nickel duplex stainless steel bars in concrete, Cement and Concrete Research. 56 (2014) 52-60.

[33] S. Ding, X. Wang, L. Qiu, Y. Ni, X. Dong, Y. Cui, A. Ashour, B. Han, J. Ou, Self-sensing cementitious composites with hierarchical carbon fiber-carbon nanotube composite fillers for crack development monitoring of a maglev girder, Small. 19 (9) (2023) 2206258.

[34] S. Ding, Y. Xiang, Y. Ni, V.K. Thakur, X. Wang, B. Han, J. Ou, In-situ synthesizing carbon nanotubes on cement to develop self-sensing cementitious composites for smart high-speed rail infrastructures, Nano Today. 43 (2022) 101438.

[35] K. Schneider, A. Michel, M. Liebscher, L. Terreri, S. Hempel, V. Mechtcherine, Mineral-impregnated carbon fibre reinforcement for high temperature resistance of thin-walled concrete structures, Cement and Concrete Composites. 97 (2019) 68-77.

[36] A. Zhou, Q.W. Qiu, C.L. Chow, D. Lau, Interfacial performance of aramid, basalt and carbon fiber reinforced polymer bonded concrete exposed to high temperature, Composites Part A: Applied Science and Manufacturing. 131 (2020).

[37] H. Wang, F.T. Shi, J.L. Shen, A.L. Zhang, L.C. Zhang, H.H. Huang, J.Z. Liu, K.K. Jin, L.Y. Feng, Z.Y. Tang, Research on the self-sensing and mechanical properties of aligned stainless steel fiber-reinforced reactive powder concrete, Cement and Concrete Composites. 119 (2021).

[38] D.L. Nguyen, M. Lam, D.J. Kim, J. Song, Direct tensile self-sensing and fracture energy of steel-fiber-reinforced concretes, Composites Part B: Engineering. 183 (2020).

[39] X. Wang, S. Ding, L. Qiu, A. Ashour, Y. Wang, B. Han, J. Ou, Improving bond of fiber-reinforced polymer bars with concrete through incorporating nanomaterials, Composites Part B: Engineering. 239 (2022) 109960.

[40] W.K. Dong, W.G. Li, N. Lu, F.L. Qu, K. Vessalas, D.C. Sheng, Piezoresistive behaviours of cement-based sensor

with carbon black subjected to various temperature and water content, Composites Part B: Engineering. 178 (2019).
[41] J. Du, W.N. Meng, K.H. Khayat, Y. Bao, P.W. Guo, Z.H. Lyu, A. Abu-obeidah, H. Nassif, H. Wang, New development of ultra-high-performance concrete (UHPC), Composites Part B: Engineering. 224 (2021).
[42] X. Wang, S. Dong, Z. Li, B. Han, J. Ou, Nanomechanical characteristics of interfacial transition zone in nano-engineered concrete, Engineering. 17 (2022) 99-109.
[43] J.H. Gong, Y.W. Ma, J.Y. Fu, J. Hu, X.W. Ouyang, Z.H. Zhang, H. Wang, Utilization of fibers in ultra-high performance concrete: A review, Composites Part B: Engineering. 241 (2022).
[44] S. Dong, B. Han, X. Yu, J. Ou, Constitutive model and reinforcing mechanisms of uniaxial compressive property for reactive powder concrete with super-fine stainless wire, Composites. Part B: Engineering. 166 (2019) 298-309.
[45] T. Sun, X. Wang, N. Maimaitituersun, S. Dong, L. Li, B. Han, Synergistic effects of steel fibers and steel wires on uniaxial tensile mechanical and self-sensing properties of UHPC, Construction and Building Materials. 416 (2024) 134991.
[46] T. Wangler, N. Roussel, F.P. Bos, T. Salet, R.J. Flatt, Digital concrete: A review, Cement and Concrete Research. 123 (2019).
[47] K. Bayraktarova, L. Eberhardsteiner, D. Zhou, R. Blab, Characterisation of the climatic temperature variations in the design of rigid pavements, International Journal of Pavement Engineering. 23 (9) (2022) 3222-3235.
[48] M.O.T. China, Specifications for Design of Highway Cement Concrete Pavement, in: JTG D40-2011, 2011, p.
[49] S. Dong, X. Wang, A. Ashour, B. Han, J. Ou, Enhancement and underlying mechanisms of stainless steel wires to fatigue properties of concrete under flexure, Cement and Concrete Composites. 126 (2022) 104372.
[50] D. Lu, Y.L. Huo, Z.S. Jiang, J. Zhong, Carbon nanotube polymer nanocomposites coated aggregate enabled highly conductive concrete for structural health monitoring, Carbon. 206 (2023) 340-350.
[51] D. Yuan, W. Jiang, A. Sha, J. Xiao, W. Wu, T. Wang, Technology method and functional characteristics of road thermoelectric generator system based on Seebeck effect, Applied Energy. 331 (2023) 120459.
[52] G. James, D. Witten, T. Hastie, R. Tibshirani, An Introduction to Statistical Learning, Springer, 2013.